remote sensing

MDPI

Article

Testing the Limits of Atmospheric Correction over Turbid Norwegian Fjords

Elinor Tessin *, Børge Hamre and Arne Skodvin Kristoffersen

Institute for Physics and Technology, University of Bergen, 5020 Bergen, Norway; borge.hamre@uib.no (B.H.); arne.kristoffersen@uib.no (A.S.K.)

* Correspondence: elinor.tessin@uib.no

Abstract: Atmospheric correction, the removal of the atmospheric signal from a satellite image, still poses a challenge over optically complex coastal water. Here, we present the first atmospheric correction validation study performed in optically complex Norwegian fjords. We compare in situ reflectance measurements and chlorophyll-*a* concentrations from Western Norwegian fjords with atmospherically corrected Sentinel-3 Ocean and Land Colour Instrument observations and chlorophyll-*a* retrievals. Measurements were taken in Hardangerfjord, Bjørnafjord and Møkstrafjord during a bright green coccolithophore bloom in May 2022, and during a period of no apparent discoloration in April 2023. Coccolithophore blooms generally peak in the blue region (490 nm), but spectra measured in this bloom peaked in the green region (559 nm), possibly due to absorption by colored dissolved organic matter ($a_{CDOM}(440) = 0.18 \pm 0.01$ m^{-1}) or due to high cell counts (up to 15 million cells/L). We tested a wide range of atmospheric correction algorithms, including ACOLITE, BAC, C2RCC, iCOR, L2gen, POLYMER and the SNAP Rayleigh correction. Surprisingly, atmospheric correction algorithms generally performed better during the bloom (average MAE = 1.25) rather than in the less scattering water in the following year (average MAE = 4.67), possibly because the high water-leaving radiances due to the high backscattering by coccolithophores outweighed the adjacency effect. However, atmospheric correction algorithms consistently underestimated water-leaving reflectance in the bloom. In non-bloom matchups, most atmospheric correction algorithms overestimated the water-leaving reflectance. POLYMER appears unsuitable for use over coccolithophore blooms but performed well in non-bloom matchups. Neither BAC, used in the official Level-2 OLCI products, nor C2RCC performed well in the bloom. Nine chlorophyll-*a* retrieval algorithms, including two algorithms based on neural nets, four based on red and near-infrared bands and three maximum band-ratio algorithms, were also tested. Most chlorophyll-*a* retrieval algorithms did not perform well in either year, although several did perform within the 70% accuracy threshold for case-2 waters. A red-edge algorithm performed best in the coccolithophore blooms, while a maximum band-ratio algorithm performed best in the following year.

Keywords: ocean color; coastal remote sensing; atmospheric correction; case-2 water; OLCI Sentinel-3; coccolithophore bloom

check for updates

Citation: Tessin, E.; Hamre, B.; Kristoffersen, A.S. Testing the Limits of Atmospheric Correction over Turbid Norwegian Fjords. *Remote Sens.* **2024**, *16*, 4082. https://doi.org/10.3390/rs16214082

Academic Editor: Raphael M. Kudela

Received: 22 August 2024
Revised: 18 October 2024
Accepted: 29 October 2024
Published: 1 November 2024

Copyright: © 2024 by the authors. Licensee MDPI, Basel, Switzerland. This article is an open access article distributed under the terms and conditions of the Creative Commons Attribution (CC BY) license (https://creativecommons.org/licenses/by/4.0/).

1. Introduction

Since the first implementation of an ocean color sensor in space in 1978 [1], ocean color remote sensing has become a vital data source for scientists monitoring the state of marine environments. It has allowed us to observe biological processes at the ocean surface at high temporal and spatial resolutions, and given access to remote areas, both in the open sea and in coastal zones.

Norwegian fjords are vulnerable to human development, e.g., aquaculture, oil drilling, hydroelectric power plants and the cruise ship industry, and remote sensing is a valuable tool to study these impacts [2,3]. The Norwegian aquaculture industry also depends on remote sensing products to monitor water quality and harmful algal blooms [4–6].

However, the uncertainties of these products can be high in coastal waters, often due to errors in atmospheric correction (with mean errors in the visible region between 13 and 25%, compared to 2% in the open ocean [7]).

Atmospheric correction is the process of removing the overwhelming majority of the signal recorded by satellite sensors (e.g., 80–90% in the blue wavelengths [8]) that is generated by molecular and aerosol scattering in the atmosphere, to retain only the comparatively weak ocean color signal. The next challenge lies in the interpretation of ocean color, for example, the retrieval of concentrations of chlorophyll-*a*, colored dissolved organic matter (CDOM) and other particulate and dissolved substances from the ocean color signal.

Atmospheric correction and the retrieval of in-water parameters are less complex in case-1, open ocean waters, where CDOM and particle concentrations generally covary with chlorophyll-*a* concentrations, and aerosols are spatially homogeneous. However, turbid, coastal waters, where ocean color is determined by a variety of substances that do not co-vary with chlorophyll-*a* concentrations, still pose a major challenge [9]. Terrigenous CDOM or inorganic, non-pigmented constituents can dominate. These constituents can be mineral particles advected from land, bubbles and even inorganic material produced by phytoplankton, e.g., coccoliths, the calcium carbonate platelets shed by coccolithophores [10].

Atmospheric correction aims to obtain the water-leaving radiance L_w (often normalized to $[L_w(\lambda)]_N$, with the sun at zenith and radiance viewed at nadir) at wavelength λ from the radiance $L_t(\lambda)$ measured by the satellite sensor [7]:

$$L_t(\lambda) = L_r(\lambda) + L_a(\lambda) + L_{ra}(\lambda) + t(\lambda)L_{wc}(\lambda) + T(\lambda)L_g(\lambda) + t(\lambda)t_0(\lambda)\cos\theta_0[L_w(\lambda)]_N \quad (1)$$

In addition to $L_w(\lambda)$, $L_t(\lambda)$ consists of the signal $L_r(\lambda)$ contributed by molecular scattering in the absence of aerosols, aerosol scattering and absorption in the absence of air molecules $L_a(\lambda)$, the interaction between aerosol and molecular scattering $L_{ra}(\lambda)$, sun glint $L_g(\lambda)$ and whitecaps $L_{wc}(\lambda)$. $t(\lambda)$ and $t_0(\lambda)$ are, respectively, the diffuse transmittances of the atmosphere between the sun and surface, and the surface and satellite sensor, θ_0 is the solar zenith angle, and $T(\lambda)$ is the direct transmittance from surface to sensor. Most atmospheric correction methods use radiative transfer models to compute the molecular scattering contribution $L_r(\lambda)$. $L_g(\lambda)$ is generally masked and can be reduced by tilting the satellite sensor, and $L_{wc}(\lambda)$ is estimated from surface windspeed. Originally, the contribution of aerosols through L_a and L_{ra} was derived from the remaining signal in the near-infrared (NIR) bands, where water-leaving radiance in clear, deep ocean water is assumed to be negligible [11]. However, turbid coastal waters with a high content of suspended materials scatter light at these wavelengths, meaning that the concentration of aerosols may be overestimated and images overcorrected when using this method.

Several atmospheric correction algorithms are available specifically for use over coastal waters. This new generation of algorithms deploys a variety of strategies to obtain the true ocean color signal, each of which has its own strengths and limitations.

Baseline Atmospheric Correction (BAC) is the algorithm used to generate the reflectances in the official Sentinel-3 OLCI Level-2 product and has been adapted for use over coastal water by estimating and removing the water-leaving NIR signal using a coupled ocean–atmosphere model [12,13]. In parallel, BAC also includes a neural network-based atmospheric correction, but only to compute in-water parameters such as chlorophyll-*a*; neural network-derived reflectances are not included in the final Level-2 product.

ACOLITE depends on dark pixels to determine aerosol optical thickness, using all available bands rather than just short-wave infrared (SWIR) and NIR bands [14]. Not relying solely on infrared bands is especially useful in coastal and inland waters, where these bands are usually contaminated by scattering from nearby land. While this method may be more accurate, it also depends on the presence of dark targets in proximity of the area of interest. The choice of subset or tile size during processing is a compromise that involves including a large enough area to contain the necessary dark targets, but not one so large that aerosol concentrations vary significantly within it.

A recent development is the use of neural networks to retrieve the surface reflectance from top-of-atmosphere (TOA) measurements (C2RCC, [15]). In this method, the limitations are determined by the training dataset of the neural network.

iCOR [16] uses soil and vegetation pixels in a scene to determine aerosol optical thickness and assumes atmospheric homogeneity over 15 × 15 km subsets of each scene but includes a correction for adjacency effects.

L2gen, the standard NASA atmospheric correction, uses radiative transfer simulations and ancillary information to correct for gaseous transmittance, white caps, Rayleigh scattering and sun glint (https://seadas.gsfc.nasa.gov, accessed on 1 May 2024). It has 14 different options for estimating aerosol contribution, of which some assume no water-leaving signal in the NIR to retrieve aerosol, as in Gordon and Wang (1994) [11], and others select an aerosol model based on Ångström coefficients and aerosol optical thickness input by the user, or directly allow the user to choose an aerosol model. The default aerosol option uses an optical model to estimate near-infrared water-leaving reflectance iteratively [17]. This option should not be used in extremely turbid waters, where its empirical optical models may not be applicable. For case-2 waters, the aerosol contribution can also be estimated from SWIR bands, as in [18]. As OLCI does not have SWIR bands, the band at 1020 nm can be chosen instead. It should be noted that the signal-to-noise ratio increases in OLCI's higher-wavelength bands, which can also increase the potential error when depending on these bands in atmospheric correction. Another option is the MUMM approach [19], which selects an aerosol model based on, among other inputs, the ratio ε of single scattering aerosol reflectance at two bands, by default, 779 and 865 nm for OLCI. This ratio should be determined and input by the user. The MUMM approach assumes the spatial homogeneity of both ratio ε and the ratio of water-leaving reflectance at the same bands.

POLYMER [20,21] uses a polynomial spectral matching technique to remove the aerosol and sun-glint signal. It does not account for CDOM variability, which can be a source of error in coastal regions, and it relies on water reflectances models that may not be valid in the region of interest or in optically complex waters, in particular. Rather than subtracting an atmospheric signal from the TOA spectrum, POLYMER returns a modelled water spectrum; this means that the resulting spectrum will always look like a realistic water spectrum but can only match in situ measurements within the scope of the model. In turbid coastal waters, the default POLYMER water reflectance model [22] has been shown to significantly underestimate reflectances [23].

Standalone Rayleigh correction methods are also available, such as the preprocessing tool in SNAP (ESA Sentinel Application Platform v9.0.0, http://step.esa.int, accessed on 1 July 2022). This method removes the molecular scattering that is estimated based on air pressure and sensor geometry [24].

Any error in the atmospheric correction will be transferred into the retrieval of chlorophyll-*a* and other in-water parameters from reflectances. However, in-water algorithms also come with their own limitations. First, approaches to estimating chlorophyll-*a* from satellite observations used empirical blue–green band-ratio algorithms. The blue–green ratio generally correlates well with chlorophyll-*a* concentrations in the open ocean, where chlorophyll-*a* generally covaries with particulate matter and CDOM, but not in coastal areas, where particulate matter and CDOM concentrations often vary independently of chlorophyll-*a* [25]. The presence of bright scatterers such as coccoliths also modifies the blue–green ratio [26]. Red-edge algorithms designed for turbid water estimate chlorophyll-*a* from the fluorescence peak in the red bands, but the chlorophyll-*a* concentrations need to be high (>10 mg m^{-3}). The two previously described neural network-based atmospheric correction algorithms, C2RCC and BAC, provide the simultaneous retrieval of water parameters such as chlorophyll-*a* concentrations, but are, again, only reliable in regions represented within the training dataset.

Although the output from atmospheric correction and chlorophyll-*a* retrieval algorithms has been validated in many turbid environments [27–31], they have not previously been tested in Norwegian coastal areas, or in the highly scattering water often seen in

Norwegian fjords during coccolithophore blooms. Coccolithophores are a group of phytoplankton with cell walls covered in calcium carbonate plates, also called coccoliths. *Emiliania huxleyi* (recently renamed *Gephyrocapsa huxleyi*, [32]), the most ubiquitous coccolithophore species, is often observed in Norwegian coastal waters. *G. huxleyi* forms intense blooms that can be easily observed both with the naked eye and in satellite images due to their bright green color, which is caused by the production and shedding of highly scattering coccoliths [26]. Shedding increases toward the end of the bloom, and the brightest blooms consist often of mostly detached coccoliths and few remaining live cells [33]. Some of the most intense *G. huxleyi* blooms reported so far have been observed in Norwegian fjords, reaching concentrations of up to 115 million cells per liter [34].

In this study, we evaluate the performance of BAC, ACOLITE, C2RCC, iCOR, POLYMER, L2gen and the SNAP Rayleigh correction, as well as nine chlorophyll-*a* retrieval algorithms [35–39], on satellite observations of Hardangerfjord, Bjørnafjord and Møkstrafjord during a bright green coccolithophore bloom in May 2022, and during a period of no apparent water discoloration in April 2023. To our knowledge, this is the first such validation study performed in Norwegian fjords.

2. Methods

2.1. Study Area

We performed in situ measurements and took water samples in three Western Norwegian fjords, Hardangerfjord and neighboring Bjørnafjord, as well as three control stations in Møkstrafjord (Figure 1).

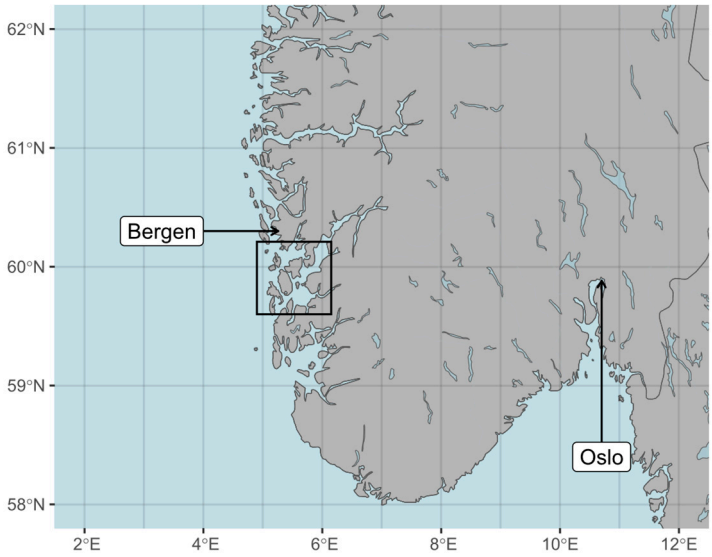


Figure 1. Partial map of Norway with the study area containing Hardangerfjord, Bjørnafjord and Møkstrafjord inside the black square.

Hardangerfjord is a large fjord in Western Norway that has experienced bright blue-green coccolithophore blooms every spring between May and July from 2019 to 2023, as visible in Sentinel-3 OLCI scenes during this time period. Optical measurements and analysis of water samples were performed during such a coccolithophore bloom in May 2022 (Figure 2) and during a period of no apparent discoloration in April 2023 (Figure 3). Stations were placed in six areas (A–F) throughout the fjords, with three stations (1–3) located at 1 km distance between them in each area.

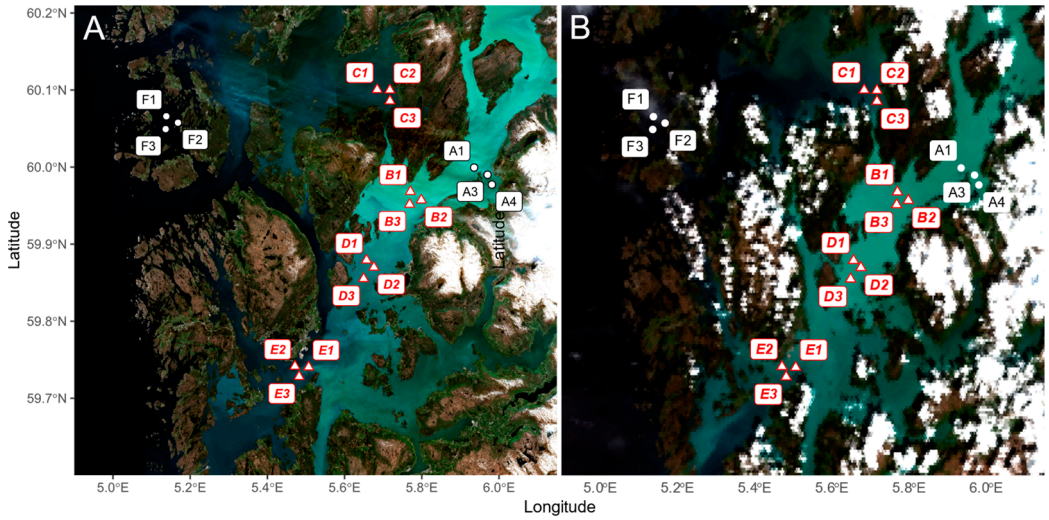


Figure 2. Sampling stations in the study area during the May 2022 coccolithophore bloom, shown on an atmospherically corrected Sentinel-2 MSI composite RGB image recorded shortly before sampling (**A**), as well as the uncorrected Sentinel-3 OLCI matchup (**B**). Stations A1, A3 and A4, B1–B3 and D1–D3 were situated inside the bloom, stations C1–C3 and E1–E3 at the bloom edge, and stations F1–F3 were control stations located outside the bloom near the open sea. Stations at which in situ reflectances were measured are marked as triangles, with labels in red, bold and italic. Chlorophyll-*a* concentration and CDOM absorption were measured at all stations.

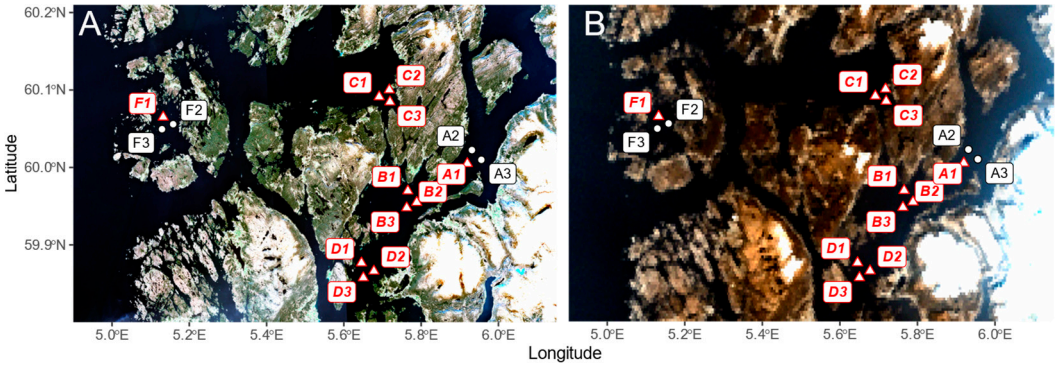


Figure 3. Sampling stations in the study area in April 2023, shown on an atmospherically corrected Sentinel-2 MSI composite RGB image recorded shortly before sampling (**A**) and the uncorrected Sentinel-3 OLCI matchup recorded on 22.04.2022 (**B**). Most 2022 stations were revisited, except station A4 and stations E1–E3. Stations at which in situ radiometry was measured are marked as triangles, with labels in red, bold and italic. Chlorophyll-*a* concentration and CDOM absorption were measured at all stations.

2.2. In Situ Data Collection

Two hyperspectral RAMSES (TriOS, Germany) radiometers were used to measure upwelling radiance and downwelling irradiance in 193 (radiance) and 191 (irradiance) channels between 320 and 950 nm. These were mounted onto a cage with 37 cm distance between each radiometer's light entrance. The cage was connected with a metal beam suspended between two flotation buoys, with the irradiance sensor floating underneath the water surface (Figure 4). The buoys were attached to the beam ends at 1.15 m from the sensors, to prevent shading. This set-up was deployed in the water for 15–30 min at each station. Continuous measurements began once the sensors had drifted far enough to assume boat shadow was not affecting the measurements, at least approximately 10 m distance from the boat. Between 40 and 130 spectra were recorded at each station, with 70 spectra on average. Radiometry measurements and the inherent optical properties

(IOPs) necessary for propagation above the surface were recorded at stations B1-3, C1-3, D1-3 and E1-3 in 2022 (Figure 2) and stations A1, B1-3, C1-3, D1-3 and F1 (Figure 3).

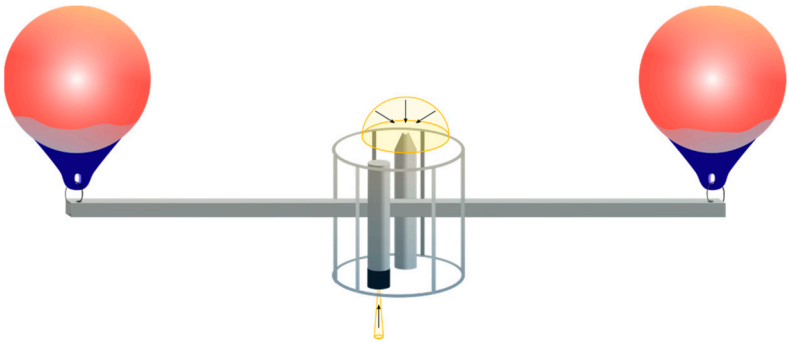


Figure 4. Radiometer set-up with radiance and irradiance sensors.

Upwelling radiance and downwelling irradiance measurements were propagated to above the surface using correction factors modelled in AccuRT [40]. These correction factors were computed as follows: below-water upwelling radiance and downwelling irradiance spectra were modelled at measurement depth using simultaneously measured IOPs, i.e., LISST-VSF phase functions, CDOM absorption spectra and suspended particulate matter (SPM) absorption spectra from UV/VIS spectrophotometer measurements. We then modelled above-surface downwelling irradiance and water-leaving radiance without the surface specular reflected component. The ratio between each modelled above- and below-surface spectrum was used as an individual correction factor by which each radiance or irradiance measurement was multiplied to propagate it to above the surface. The resulting spectra were interpolated to a 1 nm grid.

The Sentinel-3A and 3B OLCI (Ocean and Land Colour Instrument) spectral response functions $S_B(\lambda)$ were then applied to the in situ radiance and irradiance spectra as in Burggraaf (2020) [41]. The convolved radiance $\overline{L}(B)$ is computed by multiplying the measured radiance spectrum with the spectral response function of each OLCI band, integrating over all wavelengths in the band and normalizing by the integral of the band spectral response function.

$$\overline{L}(B) = \frac{\int_{\lambda \in B} L(\lambda) S_B(\lambda) d\lambda}{\int_{\lambda \in B} S_B(\lambda) d\lambda} \tag{2}$$

The convolved irradiance is similarly computed by replacing L with E in Equation (2). The remote sensing reflectance was then obtained by dividing upwelling convolved nadir radiance (subtracted specular surface reflection) by downwelling convolved irradiance, and a mean OLCI-like remote sensing reflectance spectrum was obtained for each station. The mean reflectance and corresponding mean absolute error (MAE) for each wavelength at each station were computed from the measured reflectance (Rrs_i) and total number of measured spectra ($40 \leq n \leq 130$) as follows:

$$Rrs_{mean}(\lambda) = 10^{\frac{\sum_{i=1}^{n} \log_{10} Rrs_i(\lambda)}{n}} \tag{3}$$

$$MAE\ (\lambda) = 10^{\frac{\sum_{i=1}^{n} |\log_{10} Rrs_i(\lambda) - \log_{10} Rrs_{mean}\ (\lambda)|}{n}} \tag{4}$$

In situ reflectances were not corrected for differences in solar zenith angle between the time of in situ measurement and time of satellite overpass. Using AccuRT, we modelled reflectances at both in situ and satellite solar zenith angles at each station using in-situ IOPs as input to the radiative transfer model, and observed an average MAE of 1.005 between each two spectra. The highest MAE of 1.025 was observed at stations B1, B2 and B3 in the 2022 coccolithophore bloom. We also modelled two stations (D1 in 2022, and B1 in 2023)

with the sun at zenith. The mean MAE between these spectra and those modelled with in situ measurement solar zenith angles was 1.05.

Water samples (10 L) were collected at all stations at 1 m depth to measure CDOM and SPM absorption, perform cell counts and measure chlorophyll-*a* concentrations. CDOM absorption was measured using a Liquid Waveguide Capillary Cell system (LWCC-3100, World Precision Instruments, Sarasota, FL, USA). After filtering water samples onto glass fiber filters (Whatman GF/F, 0.7 µm pore size, Sigma-Aldrich, St. Louis, MO, USA), SPM absorption was measured using the Transmittance-Reflectance method [42], on a dual-beam Shimadzu spectrophotometers with a 60 mm integrating sphere (UV-2401 PC, Shimadzu, Kyoto, Japan).

To measure chlorophyll-*a* concentrations, samples were also filtered onto glass fiber filters (Whatman GF/F, 0.7 µm pore size). The filters were then incubated in methanol to dissolve any cells and release chlorophyll-*a*. Fluorescence was measured before and after adding 10% HCl using a 10-AU Turner Designs Fluorometer (excitation/emission: 436/680 nm). This method is not the standard protocol as described in Van Heukelem and Thomas (2001) [43], which employs acetone as a solvent for extraction and uses high-pressure liquid chromatography (HPLC) to estimate chlorophyll-*a* concentrations. Instead, we follow the protocol by Holm-Hansen and Riemann (1978) [44], who use methanol due to its fast and complete pigment extraction before fluorometric measurements.

A Zeiss Axio Observer A1 microscope with 10× and 40× magnification objectives was used to image settled particles from water samples. A 10 mL sample was allowed to settle from each station, and five images were taken with each magnification. These five images were used for manual cell counting of *G. huxleyi* cells, which were identified from morphology.

Phase functions were measured in-water using a LISST-VSF (Sequoia Scientific, Bellevue, WA, USA).

2.3. Satellite Data

Sentinel-3 OLCI has a spatial resolution of 300 m, with 21 bands between 400 and 1020 nm.

Two Sentinel-3A and two Sentinel-3B OLCI scenes were identified as matchups. Level-1 and Level-2 scenes were downloaded from the Copernicus dataspace (https://browser.dataspace.copernicus.eu/, accessed on 30 April 2023, Table S1).

Matchups were defined as satellite observations ± 25.5 h from the time of the in situ measurement (Table S1). Although Seegers et al. (2018) [45] define matchups as in situ data collected within 3 h of a satellite overpass, only 11 of our stations met this criterium. To increase the size of our match-up database, we chose to include 17 stations with a larger time difference as well.

The Level-1 and Level-2 products were further processed in SNAP (ESA Sentinel Application Platform v9.0.0, http://step.esa.int, accessed on 1 July 2022). This processing included identification and masking of cloud pixels using IDEPIX (Brockmann Consult, v9.0.1) as well as atmospheric correction using the C2RCC and iCOR plugins and the Rayleigh correction included in SNAP. L2gen atmospheric correction was performed in SeaDAS (v8.4.0). ACOLITE and POLYMER atmospheric correction were performed using Python v3.10.

Matchups were then extracted as 3 × 3 pixel windows. This small window size was chosen to minimize any effect caused by adjacency to land. Windows of 5 × 5 pixels, as used in Seegers et al. (2018) [45], frequently included pixels flagged as land or coastline.

After evaluation of flags, removal of negative reflectances and visual evaluation of RGB images and spectra, only matchups with ≥5 valid pixels were included in further analysis. The mean and MAE of all 5–9 valid pixels within each window were then computed as in Equations (3) and (4) and used in further analysis.

2.4. Flags

Both IDEPIX flags and flags included in the Level-1 and Level-2 Sentinel-3 products were evaluated before analysis. Pixels were masked following EUMETSAT matchup analysis guidelines [46] as well as recommendations for the individual atmospheric correction algorithms (Table S2).

Guidelines for matchup analysis of Sentinel-3 OLCI observations also recommend exclusion of pixels flagged as CLOUD_MARGIN and HIGHGLINT in IDEPIX. In our case, coastlines within the bloom were frequently flagged as clouds and cloud margins both in the Level-2 product corrected with BAC and in the masks generated by IDEPIX. We, therefore, chose to manually review these pixels using the Level-1 and Level-2 RGB images, and included several pixels in this analysis which we consider to be erroneously flagged as CLOUD_MARGIN as no clouds were visible in the vicinity. Similarly, some matchup pixels within the bloom (B1, E1, E2 and E3, Figure 2) were flagged as HIGHGLINT in the Level-2 product. Although almost half of the respective OLCI scene was flagged as "sun_glint_risk" (determined through sensor geometry and ancillary wind speed data) in the Level-1 product, the actual area flagged HIGHGLINT in the Level-2 product is mostly restricted to and aligns well with the bright area of the coccolithophore bloom, so we again assume this to be an error in the flagging process. The corresponding L2gen glint correction flag (HIGLINT) did not flag any pixels in our matchup windows.

2.5. Atmospheric Correction

Level-1 Sentinel-3A and Sentinel-3B OLCI products were atmospherically corrected using the C2RCC, iCOR and Rayleigh correction plugins in SNAP and L2gen in SeaDAS, as well as ACOLITE and POLYMER. We also included the official Level-2 Sentinel-3 OLCI product corrected with BAC in this study (Table 1).

Table 1. Description of atmospheric correction algorithms used in this analysis, with a list of potential limitations when applied to our study area.

Algorithm	References	Method	Limitations
ACOLITE	[14,23]	Dark spectrum fitting with sun-glint correction	Needs dark pixels; assumes atmospheric homogeneity if used on subset/tiles
BAC	[12,13]	Bright pixel correction	Assumes zero water-leaving reflectance in NIR, flags very bright water pixels, limitations of training dataset for neural net products
C2RCC	[15]	Neural network	Limitations of training dataset
iCOR	[16]	Dark spectrum fitting with adjacency correction	Needs dark land pixels; assumes atmospheric homogeneity
L2gen_Std	[17,47]	Relative humidity-based model selection and iterative NIR	Fails in environments outside scope of empirical optical models
L2gen_MUMM	[19]	Aerosol model choice based on user-determined calibration parameters	Requires input of calibration parameters; assumes spatial heterogeneity of 765:865 nm ratio for aerosol and water-leaving reflectance over scene or subscene
L2gen_Wang2009	[18,48]	NIR-SWIR switching	OLCI has no SWIR band; low signal-to-noise ratio of 1020 nm band
POLYMER	[20,21]	Spectral matching with sun-glint correction	Neglects CDOM absorption variability, based on the Park and Ruddick (2005) water reflectance model [22]
Rayleigh correction	[24]	Molecular scattering estimated from air pressure and sensor geometry	No aerosol correction

BAC was originally developed for MERIS and clear waters. It was later adapted for OLCI and optically complex waters [13]. The ocean color bright-pixel correction (OC-BPC) determines and removes the contribution of marine components to the top-of-atmosphere NIR signal using a coupled ocean–atmosphere model, and flags especially bright pixels produced, e.g., by coccolithophores or bubbles (in this study, all matchup pixels from 2022 except control stations F1, F2 and F3 were flagged as white scatterers in the Level-2 product). Atmospheric correction is then performed using the clear-water atmospheric correction [12]. CWAC (Clear Water Atmospheric Correction) uses a multiple-scattering

approach to determine and remove the combined molecular and aerosol path reflectance by assuming zero water-leaving reflectance in the NIR bands centered on 779 and 865 nm. An alternative atmospheric correction using a neural network approach, similar to C2RCC, is also applied in case-2 water [49]. However, the neural network output reflectances are not made available in the Level-2 product and are only used to compute in-water parameters such as chlorophyll-*a* concentrations intended to be valid for case-2 environments. BAC was not applied locally in our study. Instead, Level-2 marine products corrected with BAC were acquired through Copernicus Dataspace (https://dataspace.copernicus.eu/, accessed on 30 April 2023) and included in our analysis. These products were not corrected for bidirectional effects (bidirectional reflectance distribution function, BRDF).

ACOLITE [14,23] was specifically designed for high-resolution coastal imagery and uses a dark-spectrum fitting approach to compute aerosol optical thickness. The same correction is then applied to the entire scene, or selected subset of the scene. We applied ACOLITE (v.20221114.0) atmospheric and glint correction to subsets of the matchup scenes (59.5 N, 5.0 E, 60.5 N and 6.5 E). ACOLITE does not include a BRDF correction.

C2RCC [15] was also originally developed for MERIS and later adapted for OLCI. It uses an artificial neural network to derive water-leaving radiance and in-water parameters. The training dataset for the neural network is comprised of water-leaving and TOA radiances simulated in HydroLight. Input spectra that are out of scope or out of range of the training dataset are flagged. C2RCC offers different neural networks for different sensors or optical environments. For Sentinel-3 OLCI, only C2RCC-Nets for general case-2 waters (v2.1) was available and was used in this study. C2RCC produces BRDF-corrected reflectances.

iCOR [16] was developed for Landsat-8 OLI and Sentinel-2 MSI and, later, modified for OLCI. The algorithm is designed to work both on land and water pixels, applying a dedicated atmospheric correction on each. It includes glint and adjacency correction (SIMEC, SIMilarity Environment Correction [50]). Aerosol optical thickness is determined for 15 × 15 km subsets of the scene, assuming atmospheric homogeneity. The darkest pixel for each band is then selected per tile and used to retrieve path radiance and estimate aerosol optical thickness using MODTRAN5 (MODerate resolution atmospheric TRANsmission, [51]) look-up tables. Aerosol optical thickness is also determined using soil and vegetation pixels. A combination of both estimates is then used to correct the image.

L2gen (https://seadas.gsfc.nasa.gov, accessed on 1 May 2024) is the standard NASA atmospheric correction processor. We tested three of its options for aerosol retrieval: the default option (Multi-scattering epsilon, relative humidity-based model selection and iterative NIR correction, abbreviated from here on as L2gen_Std; [17,47]), Multi-scattering with MUMM correction and MUMM NIR calculation (L2gen_MUMM; [19]), and Multi-scattering with 2-band model selection, (L2gen_Wang2009; [18]). The last option is designed for use with SWIR bands but was here adjusted for OLCI by using wavelengths 865 nm and 1012 nm. L2gen_MUMM was tested using a range of values for single-scattering ε. Here, only the L2gen corrections providing the best fit with each of our two sets of in situ measurements is included: L2gen_Std for both years, additionally L2gen_MUMM (ε = 0.1) and L2gen_Wang2009 for 2022, and L2gen_MUMM (ε = 1.05) for 2023. L2gen includes several options for BRDF correction. Here, we use the default option, which is based on Morel et al. (2002) [52]. L2gen_Std was additionally applied without BRDF correction.

POLYMER [20,21] (v4.16.1) fits a second-order polynomial function to the Rayleigh-corrected reflectance to remove both the aerosol and sun-glint signal. It uses the bio-optical ocean water reflectance model by Park and Ruddick (2005) [22], which includes a correction for bidirectional effects (BRDF). The model's initial parameters for chlorophyll-*a* concentration backscattering coefficients are adjusted for case-1 waters. If the model fails to converge with these parameters, the algorithm will perform a second optimization adjusted for case-2 waters.

The SNAP Rayleigh correction is based on the MERIS atmospheric correction. It removes molecular scattering estimated from air pressure and sensor geometry [24].

Not all the atmospheric correction algorithms described here include a BRDF correction, which aims to convert off-nadir satellite radiance measurements into nadir-viewing water-leaving radiance. Given that we measured nadir-viewing radiances in situ, we chose to use BRDF correction when included within the atmospheric correction algorithm. However, as there is no current consensus on which of the various BRDF correction methods is most suitable for case-2 water, we applied no separate BRDF correction when it was not included in the atmospheric correction processor. C2RCC, L2gen and POLYMER included BRDF correction, while ACOLITE, BAC, iCOR and the SNAP Rayleigh correction did not.

System vicarious gains were not applied to all atmospherically corrected products. Both OLCI-A and OLCI-B TOA measurements have a positive bias (up to 3% in the visible bands for OLCI-A, 2% for OLCI-B [53]). Gains are computed as the ratio between expected and remotely measured radiance and should be applied before atmospheric correction. Gains are specific not only to the sensor but also to each atmospheric correction processor, and they are usually computed with matchups from low-signal, oligotrophic waters. In turbid, coastal regions, this may be a source of error [54]. In this study, processor-specific gains were available and applied to BAC, L2gen and POLYMER. BAC-specific gains were also applied to ACOLITE and C2RCC following processor default settings.

2.6. Chlorophyll-a Retrieval Algorithms

The atmospherically corrected reflectances were used to compute chlorophyll-*a* concentrations with nine different chlorophyll-*a* algorithms. These included four red-edge algorithms [35–38,55,56] and three band-ratio algorithms (OC4, OC5, OC6; [39]). In addition to these, the OC4ME and neural network chlorophyll-*a* concentration estimates computed by BAC and C2RCC were also included in the analysis.

The red-edge algorithms use either two [37] or three [35,36,38,55,56] bands in the red and NIR. All of them have been designed for use in coastal and inland waters and use the OLCI band at 709 nm. Estimating chlorophyll-*a* from the red and NIR bands reduces the effect of CDOM absorption, which, in coastal regions, often does not covary with chlorophyll-*a* and decreases approximately exponentially with increasing wavelength [57].

The band-ratio algorithms use between four and six bands in the visible region, as indicated in their respective names, together with empirically derived coefficients [39]. OC4, OC5 and OC6 all use the OLCI bands at 443 nm, 490 nm, 510 nm and 560 nm. OC5 and OC6 in addition use the 412 nm band, and OC6 also uses the band at 665 nm. All three algorithms use a maximum band-ratio, i.e., choose the band with the highest signal below 560 nm, and divide this by the signal at 560 nm, or in the case of OC6, divide by the average signal of the 560 nm and 665 nm bands.

The neural network algorithms use all available bands to retrieve inherent optical properties and from these, TSM and chlorophyll-*a* concentrations [15,49].

2.7. Analysis

Following the recommendations of Seegers et al. (2018) [45], we evaluated atmospheric correction performance using mean absolute error (MAE) and bias. The MAE is a measure of accuracy that shows error magnitude without amplifying outliers. An MAE close to 1 shows good agreement between satellite retrievals and in situ measurements. The bias estimates the direction of error through the average difference between the mean satellite retrieval and mean in situ measurement. A bias larger than 1 shows overestimation, while a bias lower than 1 shows underestimation.

$$MAE\ (\lambda) = 10^{\frac{\sum_{i=1}^{n} |\log_{10} Rrs_{\ i\ (Sat)}(\lambda) - \log_{10} Rrs_{i\ (in\ situ)}(\lambda)|}{n}}, \quad (5)$$

$$bias\ (\lambda) = 10^{\frac{\sum_{i=1}^{n} \log_{10} Rrs_{i\ (Sat)}(\lambda) - \log_{10} Rrs_{i\ (in\ situ)}(\lambda)}{n}} \quad (6)$$

We also evaluated the number of valid retrievals per atmospheric correction and band, or atmospheric correction and chlorophyll-*a* algorithm. To identify the overall

best performance, we conducted a pairwise comparison. For each reflectance band or chlorophyll-*a* match-up, we calculated the difference between satellite retrieval and in situ measurement. All algorithms were then compared pairwise, and for each matchup (and if applicable, band), the atmospheric correction algorithm, or combination between atmospheric correction algorithm and chlorophyll-*a* algorithm, with the smaller absolute difference was then designated the winner. The percentage of wins was computed by dividing the total number of wins for each algorithm by the number of possible wins. Algorithms were then evaluated by their percentage of wins.

3. Results

3.1. In Situ Chlorophyll-a, $a_{CDOM}(440)$ and Cell Counts

We observed clear differences in chlorophyll-*a* concentrations inside and outside the coccolithophore bloom in 2022 (Figure 5). Chlorophyll-*a* concentrations were highest in the center of the coccolithophore bloom (6.9 $\pm$ 0.9 mg m^{-3}), decreased slightly towards the edge (5 $\pm$ 1 mg m^{-3}), and were very low at the control stations outside the bloom (1.1 $\pm$ 0.2 mg m^{-3}). In April 2023, chlorophyll-*a* concentrations were lower throughout the sampling area, but slightly higher in the inner fjord (2.8 $\pm$ 0.5 mg m^{-3}) compared to the outer fjord (1.7 $\pm$ 0.2 mg m^{-3}), or the control stations in Møkstrafjord (1.9 $\pm$ 0.5 mg m^{-3}).

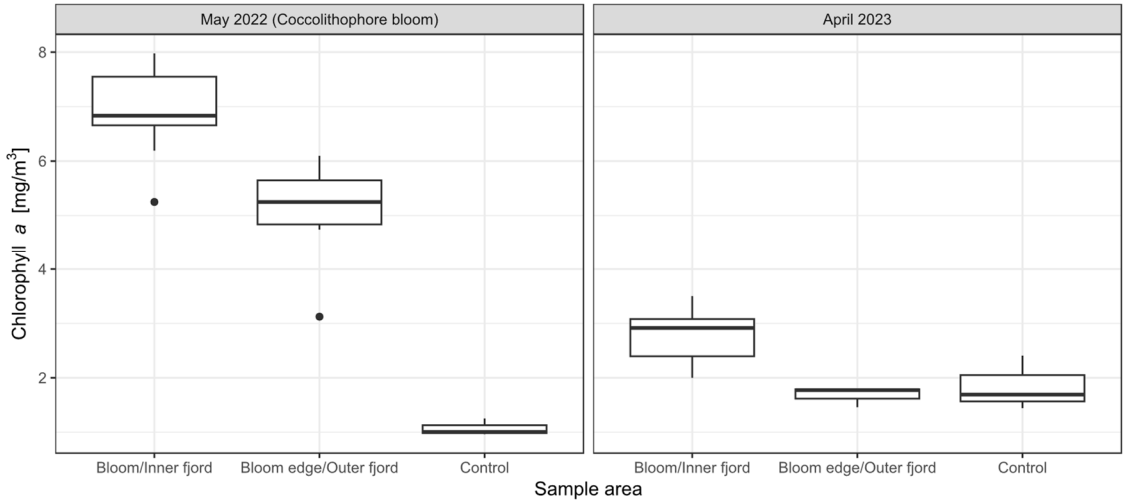


Figure 5. Chlorophyll-a concentrations measured in the study area in May 2022 and April 2023. Sampling stations were divided into "bloom/inner fjord" (stations A1-3, B1-3 and D1-3), "edge/outer fjord" (C1-3 and E1-3) and control (F1-3).

CDOM absorption at 440 nm was high in the center of the bloom (0.18 $\pm$ 0.01 m^{-1}, Figure 6), and decreased toward the control stations (0.09 $\pm$ 0.01 m^{-1}), similar to chlorophyll-*a* concentrations. In April 2023, CDOM was lower throughout most of the sampling area (<0.1 m^{-1}).

G. huxleyi cell counts recorded in 2022 ranged between 0.7 $\times$ 10^6 cells/L at station F1 and 15 $\times$ 10^6 cells/L at station A1. Only very few detached coccoliths were observed at 40$\times$ magnification, and none were observed at 10$\times$ magnification.

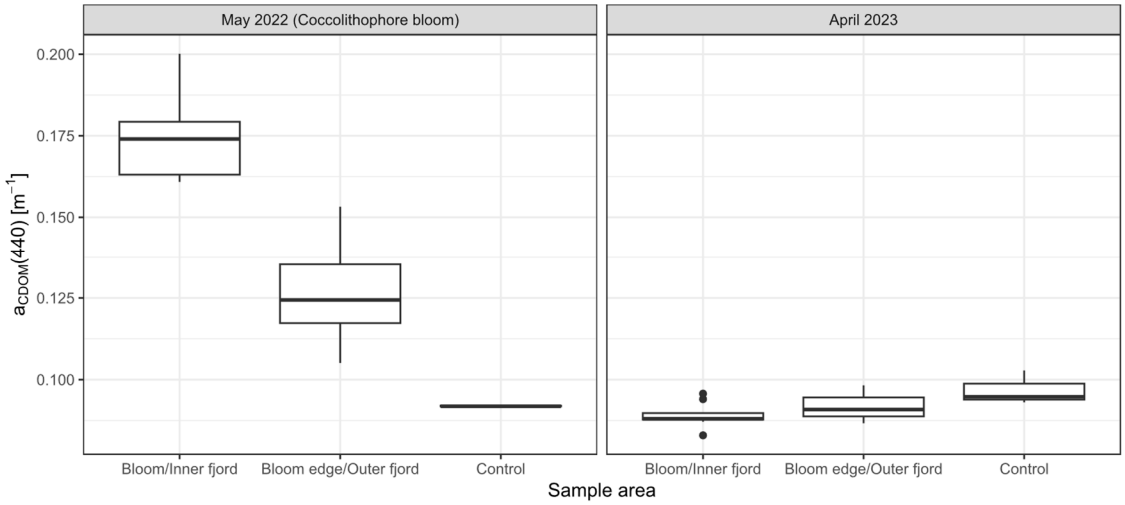


Figure 6. CDOM absorption at 440 nm measured in the study area in May 2022 and April 2023. Sampling stations were divided into "bloom/inner fjord" (stations A1-3, B1-3 and D1-3), "edge/outer fjord" (C1-3 and E1-3) and control (F1-3).

3.2. In Situ Reflectances

In situ reflectance spectra measured in the 2022 coccolithophore bloom were bright, with a peak R_{rs} = 0.033 ⁎ 1.6 sr^{-1} (MAE) at 542 nm, where the division-times symbol ⁎ indicates that the mean value should be divided and multiplied with the succeeding factor to obtain the value range. The R_{rs} peaked in the green region at 559 nm in the center of the coccolithophore bloom, and at 540 nm at the edge of the bloom (Figure 7). In April 2023, spectra peaked in the blue to green regions (502 nm in the inner fjords, and 489 nm at the control stations) and were one order of magnitude lower in brightness, with a peak R_{rs} = 0.0024 ⁎ 1.3 sr^{-1} at 489 nm.

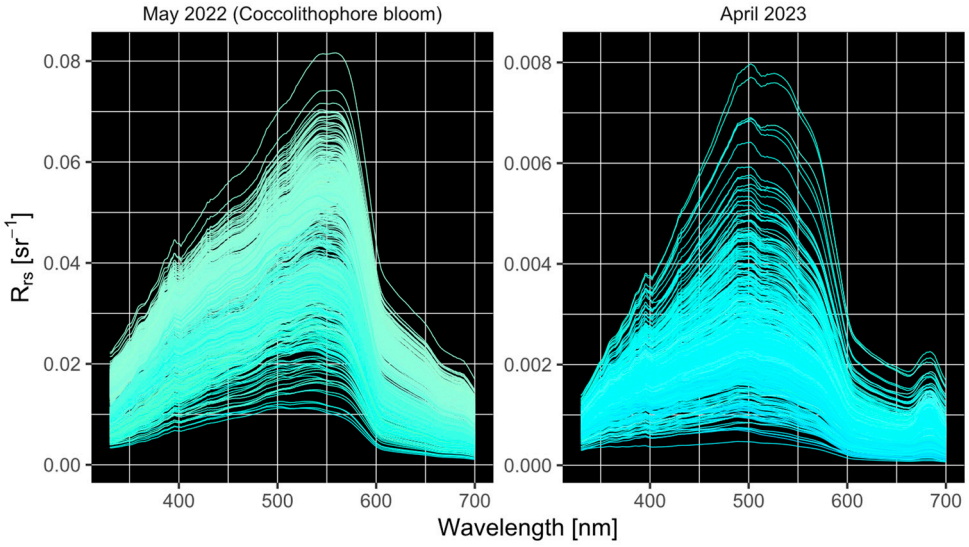


Figure 7. In situ reflectance spectra measured in the study area during the May 2022 coccolithophore bloom (stations B1-3, C1-3, D1-3 and E1-3) and in April 2023 (stations A1, B1-3, C1-3, D1-3 and F1). Each spectrum is colored in its respective RGB color. RGB colors were obtained by weighting each reflectance spectra with the CIE tristimulus functions, integrating the three resulting curves and scaling to 1.

3.3. Remote Sensing

3.3.1. Remote Sensing Reflectances

We identified 11 ± 1-day cloud-free matchups of in situ radiometry measurements with one Sentinel-3A OLCI image during the 2022 coccolithophore bloom (B1-3, C1-3, D1-3, E1 and E3), as well as 8 ± 1-day (A1, B1-3, C1-3 and F1) and 3 > 1-day matchups (D1-3) with two Sentinel-3B images and one Sentinel-3A image in April 2023 (Table S1, Figures 2, 3, S2 and S3). Quality flags were applied (Table S2) and negative reflectances removed. In 2023, all corrected products except Rayleigh and C2RCC showed negative reflectances in several bands, most often between 665 and 709 nm, which were removed from further analysis. L2gen_Std only made a single positive retrieval at 674 nm and 709 nm, and BAC only two. To avoid effectively eliminating these algorithms from further analysis, we only removed the negative bands rather than the whole spectrum.

As a measure of variability within the 3 × 3 pixel windows, we computed MAEs between pixels as in Equation (4). Mean MAE was 1.01 in both years.

In the 2022 coccolithophore bloom, in situ measured water-leaving reflectance constituted between 38% (at 400 nm) and 93% (560 nm) of the TOA reflectance, while in 2023, water-leaving reflectance only accounted for between 2.5% (400 nm) and 9.9% (560 nm) of the TOA reflectance.

No atmospheric corrections were able to match both the shape and magnitude of the in situ spectra measured inside the coccolithophore bloom, either underestimating reflectances and peak height, or overestimating reflectances at all bands (Figure 8). C2RCC produced a peak at 490 nm at eight stations, far off from the in situ measured spectra which peaked between 540 and 559 nm. While other corrected spectra were more similar to in-situ spectra in shape, they did not match well in magnitude. ACOLITE overestimated reflectances in the blue bands at nine of 11 stations. POLYMER returned the lowest reflectances at eight stations. In 2023, all atmospheric corrections except BAC, POLYMER and L2gen_Std far overestimated reflectance in the blue bands (Figure 9). L2gen_Std performed slightly better without BRDF correction (mean MAE = 1.2 with BRDF, mean MAE = 1.1 without BRDF in 2022, mean MAE = 1.9 with BRDF, 1.8 without BRDF in 2023). In the following plots, we will only show reflectances corrected with default L2gen_Std settings, i.e., with BRDF correction (Figures 8–11).

It is well known that both spatial and temporal variability of in situ reflectance can significantly impact the accuracy of satellite matchups, particularly in coastal and estuarine environments [58]. To estimate how reflectances may have changed between our in-situ measurements and the corresponding satellite measurements due to bloom and water mass dynamics, we also extracted matchups from the next available Sentinel-3A OLCI Level-2 scene taken during the coccolithophore bloom on May 22nd, two days after the Sentinel-3A OLCI image used in this study (Figure 2). Only three of our stations were cloud-free (≥5 unflagged pixels) in this scene.

We calculated MAE values for spectra 48 h apart to be in the range 1.004–1.15, with a median MAE of 1.06. Given that the maximum match-up time for the compared spectra in this study is 25.5 h, the observed errors from the 48 h comparison likely represent an extreme upper bound of the variability between in situ and satellite-derived reflectance.

Both MAE and bias were lower, on average, in 2022 (MAE = 1.2, bias = 0.9) compared to 2023 (MAE = 2.6, bias = 2.0). In observations of the coccolithophore bloom, most atmospheric correction algorithms showed a bias < 1, overcorrecting the spectrum (Figure 10). The two exceptions to this were ACOLITE and the SNAP Rayleigh correction (both with average bias = 1.2), which showed a positive bias in all bands. At 560 nm, Rayleigh-corrected reflectance corresponded extremely well with in-situ reflectance measurements (bias = 1.02, wins = 98%). POLYMER showed the largest negative bias in all but three bands, underestimating reflectances by up to 32%, and the smallest percentage of wins in six out of the 10 evaluated bands. L2gen_Wang showed the highest percentage of wins in five out 10 bands, with iCOR and the Rayleigh correction winning the remaining bands.

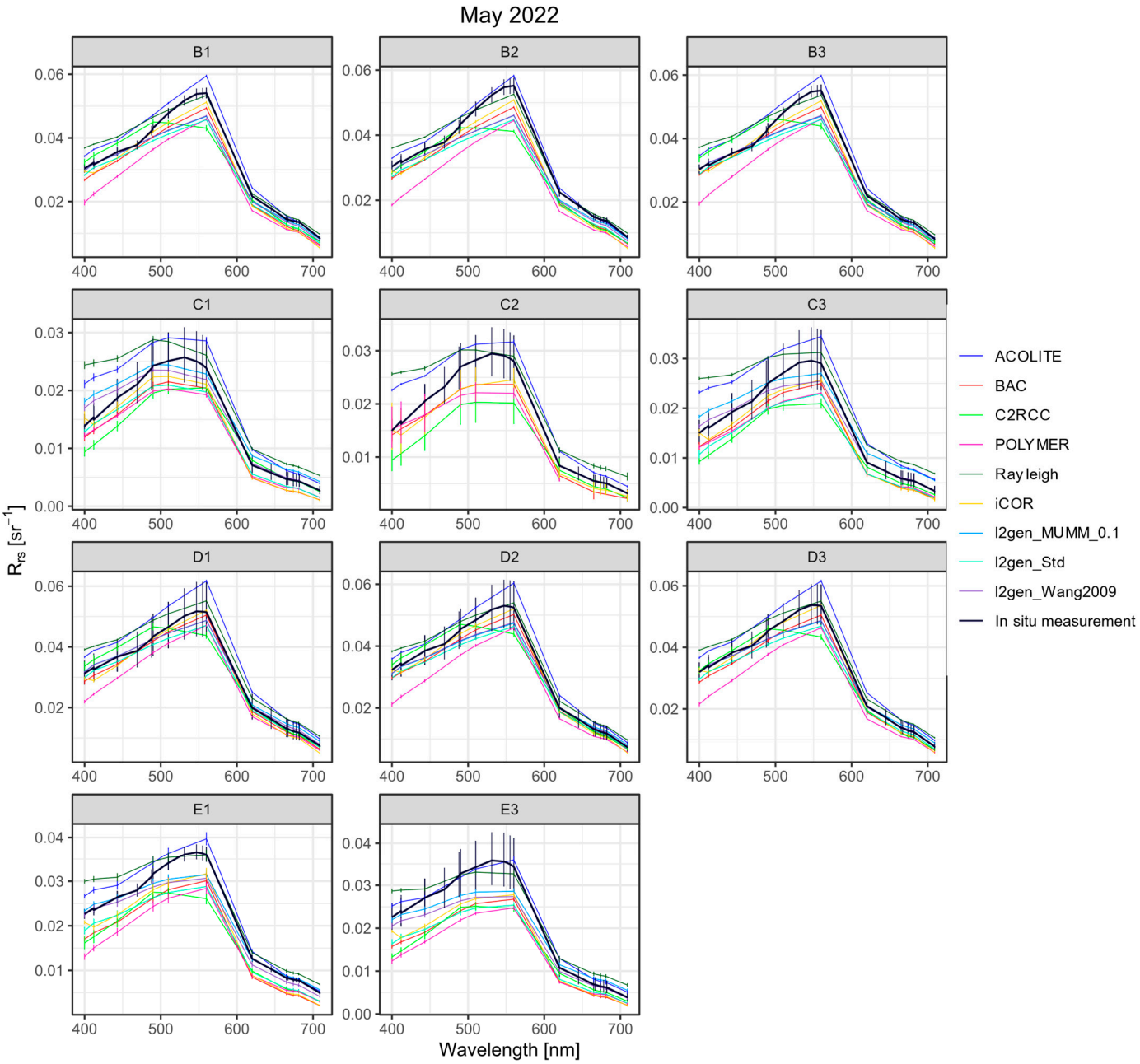


Figure 8. SRF-convolved in situ reflectances and OLCI reflectances obtained using different atmospheric corrections during the coccolithophore bloom in May 2022. The atmospheric correction algorithms are further described in Section 2.5 and Table 1. Error bars show the mean (Equation (3)) in situ or OLCI reflectance multiplied and divided by MAE (Equation (4)).

In 2023, the Rayleigh correction and iCOR showed strong positive bias, especially in the blue bands (respectively 8.3 and 5.9 at 400 nm, Figure 11). All other algorithms except L2gen_Std and POLYMER also showed a smaller positive bias. POLYMER had the highest percentage of wins and lowest MAE in five out of 10 bands, although L2gen_MUMM, C2RCC, ACOLITE and iCOR all performed better in wavelengths > 560 nm.

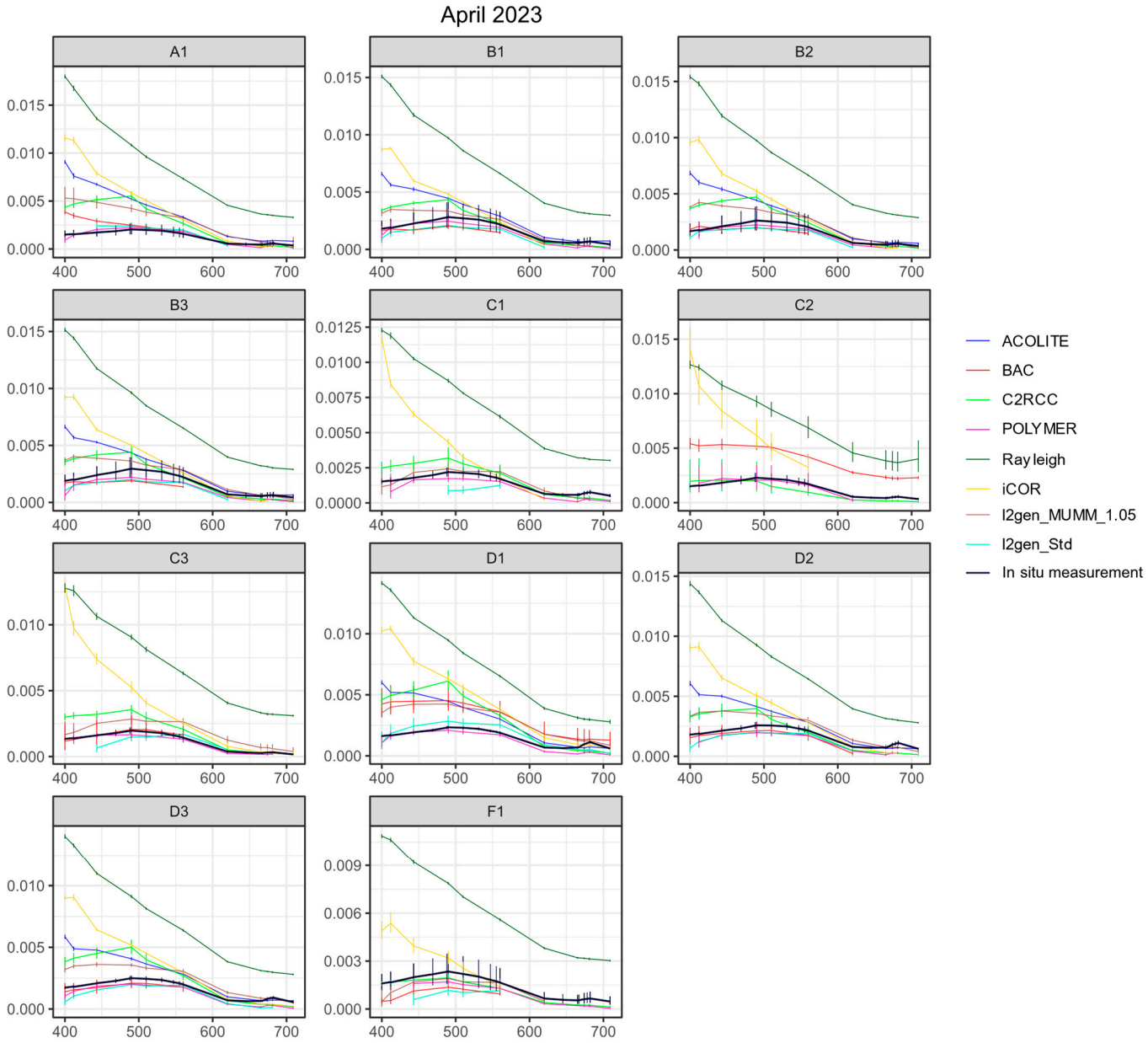


Figure 9. SRF-convolved in situ reflectances and OLCI reflectances obtained using different atmospheric corrections during April 2023. The atmospheric correction algorithms are further described in Section 2.5 and Table 1. Error bars show mean (Equation (3)) in situ or OLCI reflectance multiplied and divided by MAE (Equation (4)).

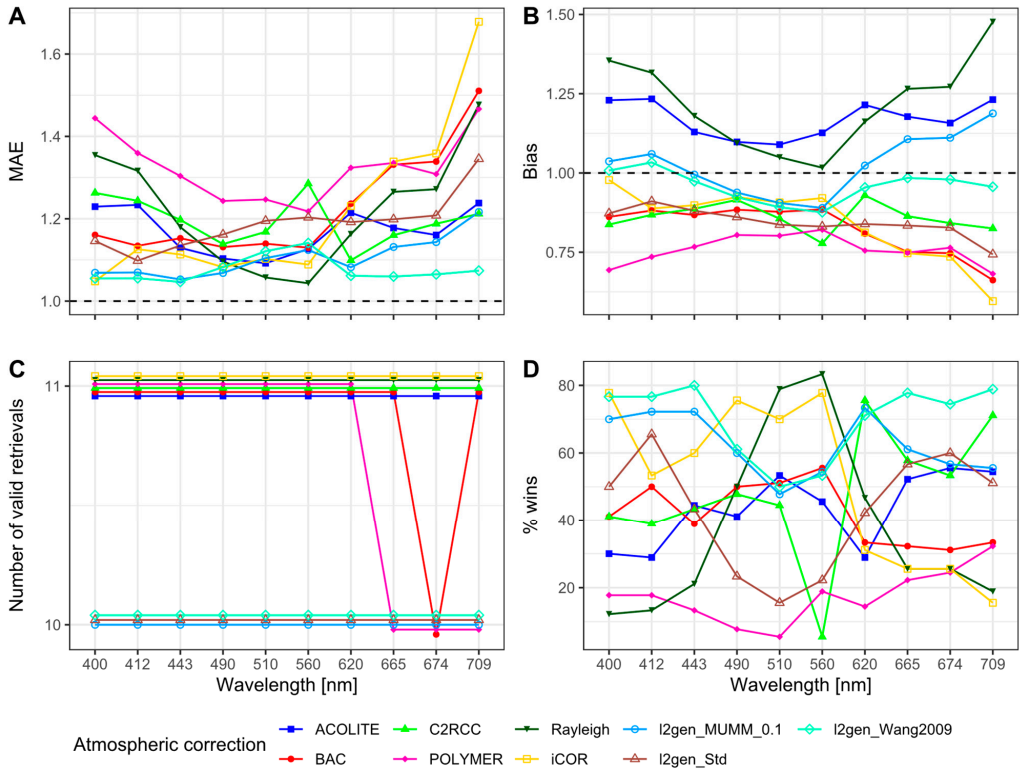


Figure 10. MAE (**A**), bias (**B**), number of valid retrievals (**C**) and percentage of wins in pairwise comparison (**D**) for all radiometry matchups recorded in the 2022 coccolithophore bloom.

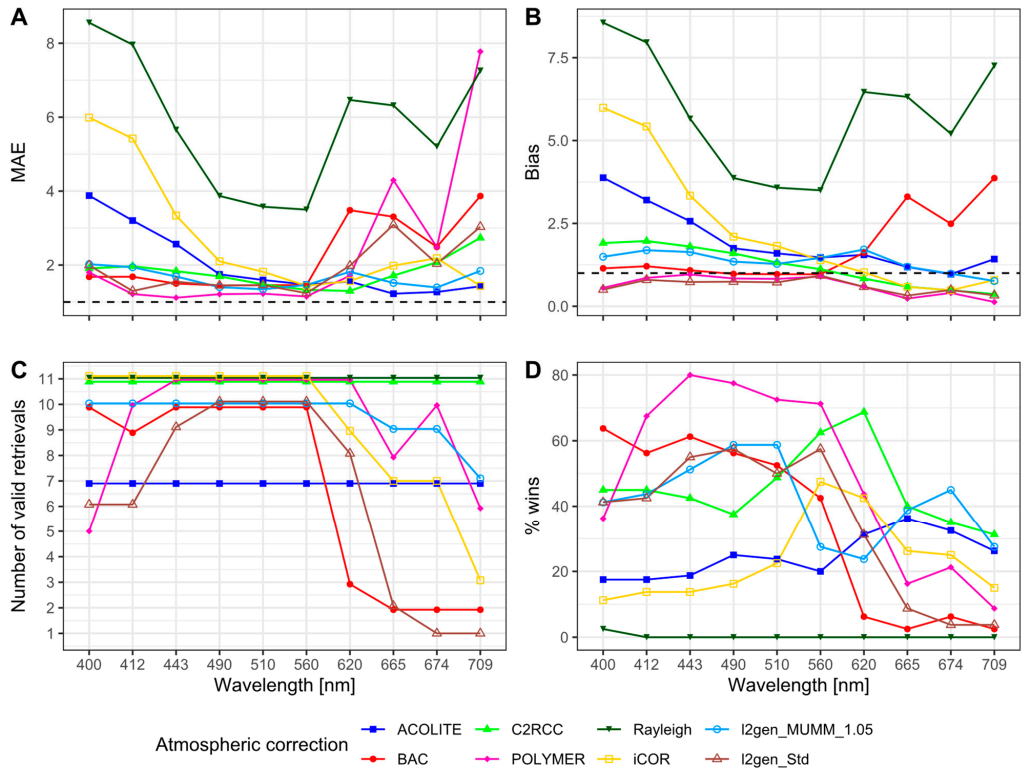


Figure 11. MAE (**A**), bias (**B**), number of valid retrievals (**C**) and percentage of wins in pairwise comparison (**D**) for all radiometry matchups recorded in April 2023.

3.3.2. Chlorophyll-*a*

We identified 13 matchups of in situ chlorophyll-*a* measurements with one Sentinel-3A OLCI image during the May 2022 coccolithophore bloom (A2, A3, B1-3, C1-3, D1-3, E1 and E3), as well as 12 ± 1-day and 3 ± 2-day matchups (A1-3, B1-3, C1-3, D1-3 and F1-3) with two Sentinel-3B images and one Sentinel-3A image in April 2023.

Red-edge algorithms, particularly those from Bramich et al. 2021, Gons et al. 2005 and Moses et al. 2019 [35,36,38], gave fewer valid retrievals (chlorophyll-*a* concentrations ranging from 0 to 100 mg m^{-3}) than band-ratio and neural net algorithms in either the coccolithophore bloom or the following year (Figures 12–15). We found better agreement between chlorophyll-*a* in situ measurements and remote sensing retrievals during the 2022 bloom than in 2023, with lower MAE (mean MAE = 1.8 in 2022, 3.4 in 2023) and bias (mean bias 0.7 in 2022, 2.06 in 2023, Figures 14 and 15). Remote sensing retrievals were negatively biased in 2022; however, Mishra and Mishra (2012) and Moses et al. (2019) [37,38] showed positive bias in combination with iCOR and BAC. Red-edge algorithms were positively biased in 2023, while neural nets and band-ratio algorithms showed a slight negative bias.

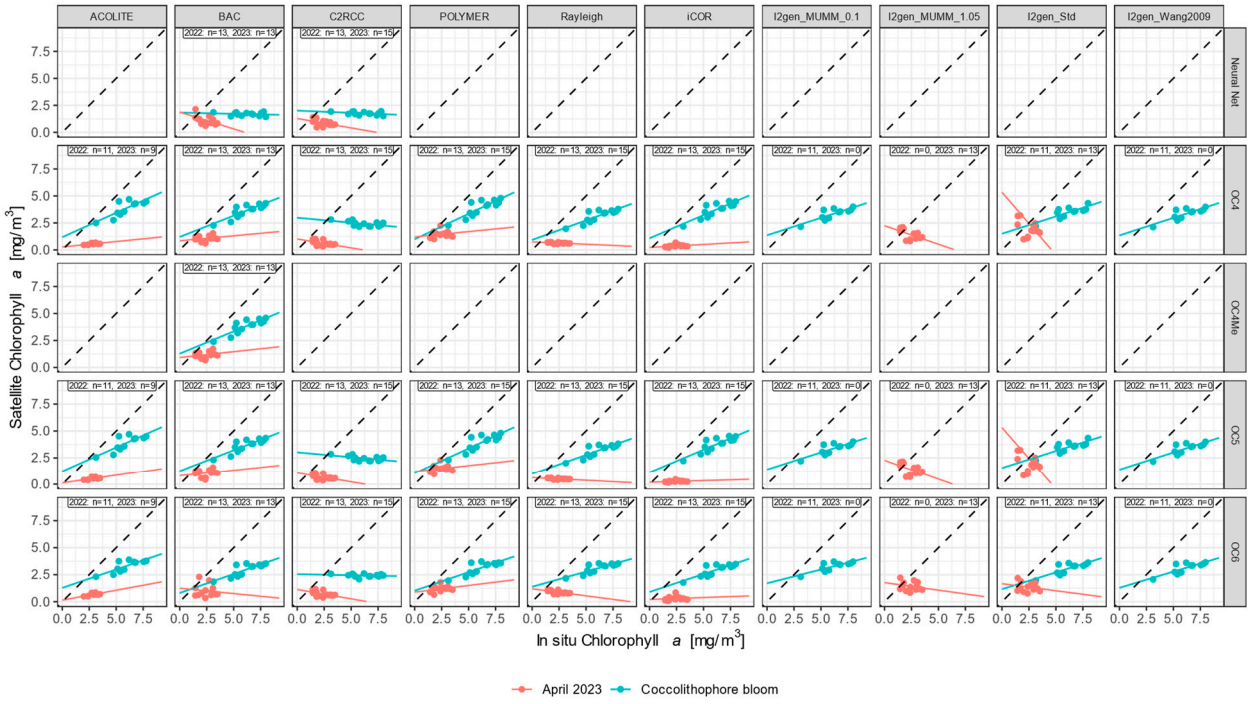


Figure 12. In situ chlorophyll-*a* concentrations compared to concentrations computed from OLCI reflectances, using the C2RCC and BAC neural net algorithms as well as 4 blue-green band-ratio algorithms. 1:1 lines are shown as dashed, while linear regression fits for each atmospheric correction and chlorophyll-*a* algorithm are shown in red for 2022 retrievals and blue for 2023 retrievals. Negative values and extreme outliers (>100 mg/m^3) were removed. Plots are labelled with the respective number of valid retrievals. Note that the neural net product was only computed by BAC and C2RCC, and OC4Me only by BAC.

After removing negative values and outliers above 100 mg m^{-3}, the best match with in-situ values was produced by the Mishra and Mishra (2012) [37] algorithm in combination with C2RCC-corrected satellite reflectances (wins = 85%), closely followed by combinations with other atmospheric correction algorithms. In 2023, band-ratio algorithms had a higher percentage of wins than all other algorithms, with the overall winner being POLYMER in combination with OC5 (wins = 91%).

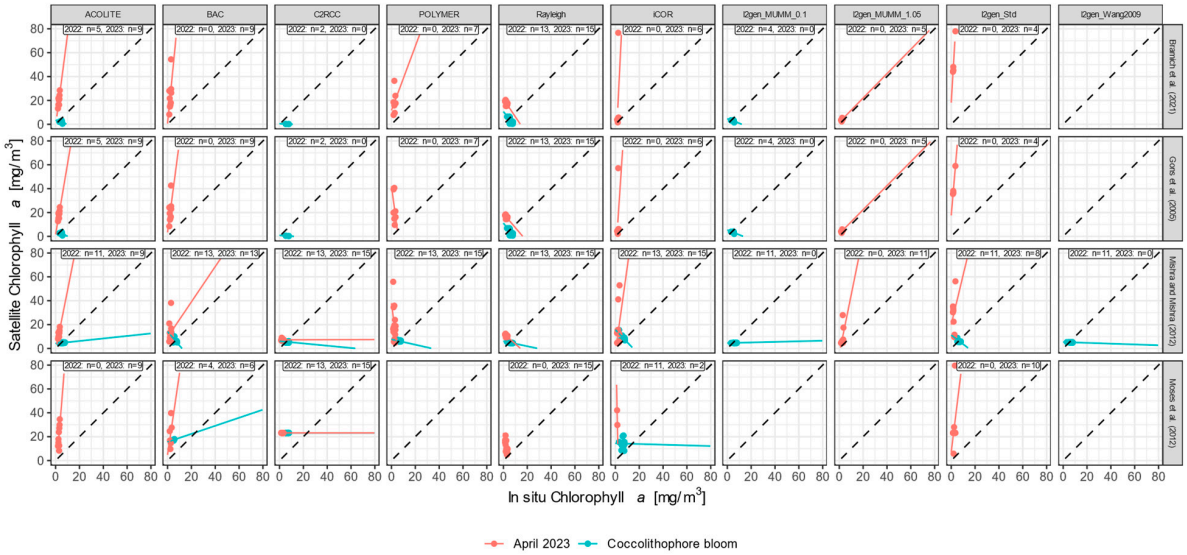


Figure 13. In situ chlorophyll-*a* concentrations compared to concentrations computed from OLCI reflectances, using four red-edge algorithms [35–38,55,56]. 1:1 lines are shown as dashed, while linear regression fits for each atmospheric correction and chlorophyll-*a* algorithm are shown in red for 2022 retrievals and blue for 2023 retrievals. Negative values and extreme outliers (>100 mg/m^3) were removed. Plots are labelled with the respective number of valid retrievals. Note that L2gen_Mumm_0.1 and L2gen_Wang2009 atmospheric corrections were only applied to 2022 data, and L2gen_MUMM_1.05 only to 2023 data. Any other missing data is due to retrieved chlorophyll-*a* concentrations being negative or >100 mg m^{-3}.

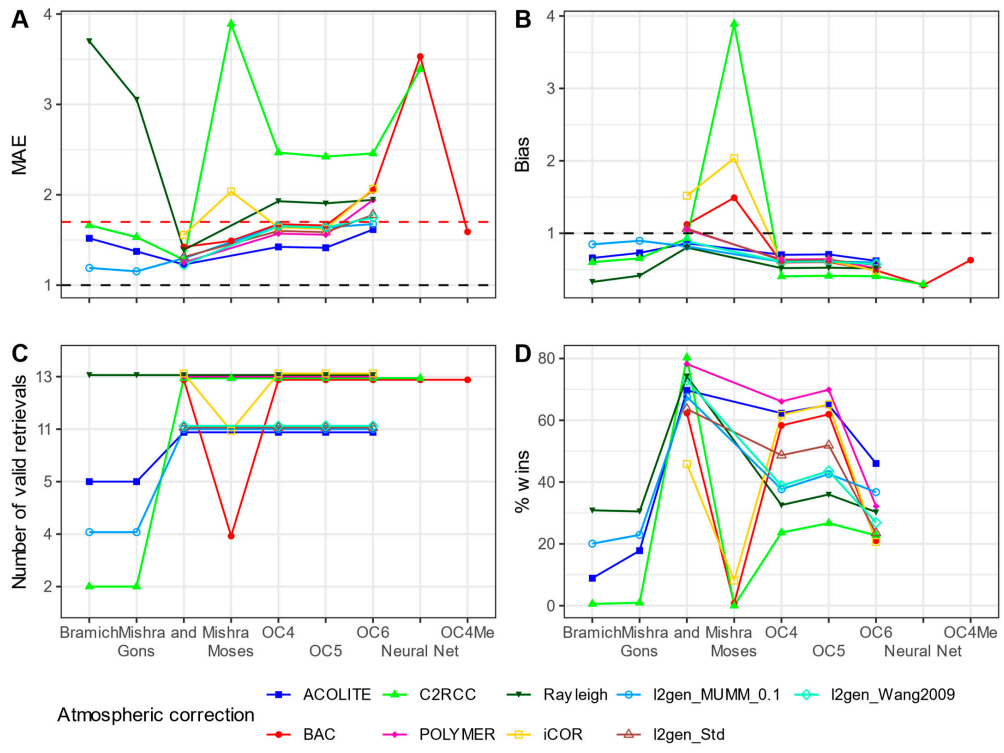


Figure 14. MAE (**A**), bias (**B**), number of valid retrievals (**C**) and percentage of wins (**D**) in pairwise comparison for all chlorophyll-*a* matchups recorded in the 2022 coccolithophore bloom. Neural net and OC4Me chlorophyll-*a* retrievals were not included in the pairwise comparison (**D**). The red dashed line in the MAE plot shows the OLCI ocean color mission threshold of 70% accuracy for chlorophyll-*a* in case-2 water [59].

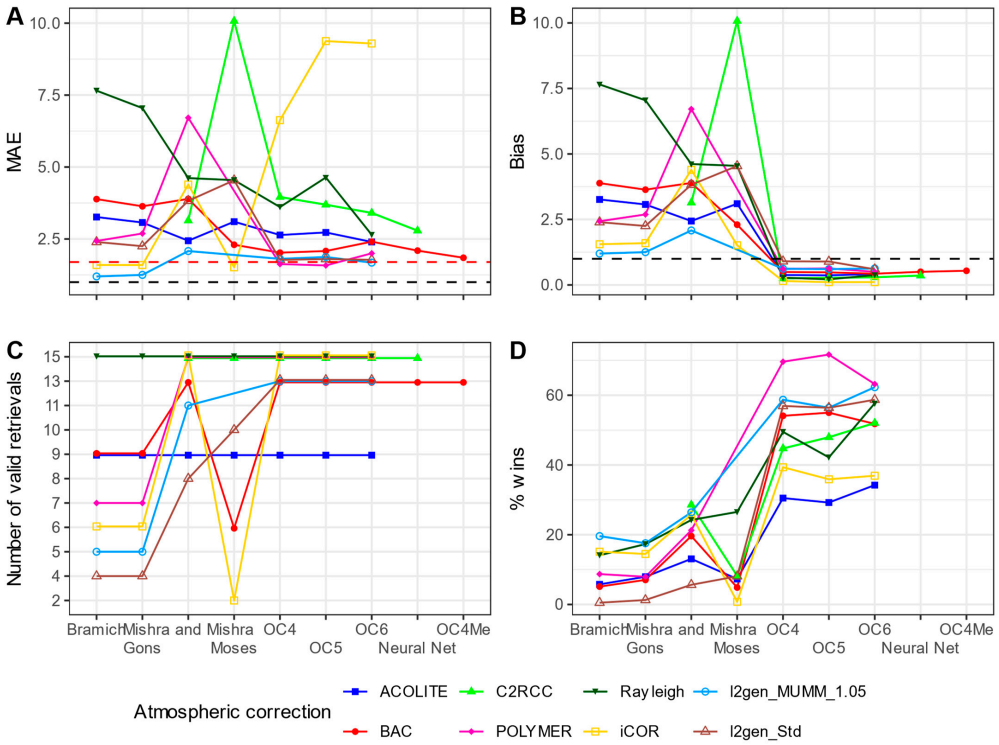


Figure 15. MAE (**A**), bias (**B**), number of valid retrievals (**C**) and percentage of wins (**D**) in pairwise comparison for all chlorophyll-*a* matchups recorded in April 2023. Neural net and OC4Me chlorophyll-*a* retrievals were not included in the pairwise comparison (**D**). The red dashed line in the MAE plot shows the OLCI ocean color mission threshold of 70% accuracy for chlorophyll-*a* in case-2 water [59].

4. Discussion

We have tested the performance of the most widely used atmospheric correction and in-water algorithms on observations of Norwegian fjords, both during a bright green coccolithophore bloom and during a period of no apparent discoloration in April 2023. However, our findings and recommendations are also relevant for other coastal waters with high concentrations of absorbing material or scattering particles.

Coccolithophore blooms are generally characterized by their bright blue color, with a reflectance peak at 490 nm, both in remote sensing and in situ measurements [60]. Contrary to that, we observed peaks at 559 nm (in-situ) and 560 nm (OLCI) in the center of the bloom (Figures 7 and 8). Due to their unusual color, these observations fell outside of the radiance thresholds defined by Brown and Yoder (1994) [61] and failed to be flagged as coccolithophore bloom pixels in L2gen, while pixels at the edge of the bloom, where reflectance was shifted towards the blue, were flagged.

Although rare, other studies have made similar observations in blooms where other algal species, or high concentrations of CDOM or non-algal particles, modified the ocean color. Garcia et al. (2011) [62] observed spectra peaking at 540 nm in the Patagonian shelf region at stations with both coccolithophores and diatoms. Similarly, Siegel et al. (2007) [63] found that SeaWIFS spectra in coccolithophore blooms peaked at 550 nm when diatoms and dinoflagellates were also present. In our case, the reflectance was modified by the elevated CDOM absorption recorded in the inner fjord and center of the bloom (Figure 6). Very high cell counts (up to 15×10^6 cells/L) with few detached coccoliths, as observed in the center of the bloom, could also contribute to a shift towards the green.

Spatial and temporal mismatches between in situ and satellite observations always pose a problem in validation studies, but even more so in our case. Only 11 of our 28 matchups lay within 3 h of the associated satellite measurement. The Western Norwegian coast is notoriously cloudy, and cloud-free satellite matchups are extremely rare. It is likely that this temporal mismatch contributed to the differences we observed between

in-situ and satellite reflectances in this study. After comparing two subsequent Sentinel-3 OLCI images taken during the coccolithophore bloom, we observed that matchup reflectances changed by a factor of ⁎1.06 (MAE) on average during the 48 h between the two images due to bloom dynamics or movement of water masses. This may explain some, but not nearly all, of the difference between the in situ and satellite reflectances observed in this study (mean MAE for all atmospheric corrections = 1.2 in 2022). Given that in this study, 25.5 h at most and 9 h on average passed between the in-situ measurement and satellite overpass, these values represent an upper bound of temporal variability in the study region.

Surprisingly, the increased ocean-leaving signal during the coccolithophore bloom seemed to improve the reflectance matchup quality (average MAE = 1.25) compared to the less scattering water in the following year (average MAE = 4.67), perhaps because increased water-leaving signal reduces the proportional effect of land adjacency on the TOA signal. The higher MAE and bias between in situ and satellite reflectances in the April 2023 matchups can be explained by the reduced water signal due to clearer water and lower backscattering, and higher solar zenith angles (40.6° ± 0.1 in May 2022, compared to 50.3° ± 0.4 in April 2023) as well as higher observation zenith angles (14.2° ± 0.5 in May 2022, 23.7° ± 6.3 in April 2023). In the coccolithophore bloom, the in situ measured reflectance constituted up to 93% (at 560 nm) of the TOA reflectance, while in the less scattering waters, it made up only up to 9.9%. In these conditions, adjacency effect from nearby land may dominate, especially in the narrow fjords of our study region. However, we observed a strong negative bias from all atmospheric corrections except ACOLITE and Rayleigh during the 2022 bloom. POLYMER stood out as especially biased, removing on average 24% of the water-leaving reflectance. In 2023, atmospheric correction algorithms were generally positively biased, except POLYMER and L2gen, which showed negative bias at all wavelengths.

In 2022, during the coccolithophore bloom, algorithms with and without BRDF correction performed similarly (mean MAE = 1.2 both with and without BRDF). In 2023, atmospheric correction algorithms with BRDF correction (C2RCC, L2gen and POLYMER) performed, on average, better than those without (BAC, ACOLITE and iCOR; mean MAE = 1.8 with BRDF, mean MAE = 2.1 without BRDF). We tested one algorithm, L2gen_Std, with and without the default BRDF correction based on Morel et al. (2002) [52]. This algorithm performed slightly better without BRDF correction both during the coccolithophore bloom in 2022 (mean MAE = 1.2 with BRDF, mean MAE = 1.1 without BRDF) and in 2023 (mean MAE = 1.9 with BRDF, 1.8 without BRDF). However, this BRDF correction method is parameterized for oceanic waters, and its failure in more optically complex coastal water is not surprising.

We did not expect C2RCC to be well-suited for use over coccolithophore blooms due to the current limitations of its neural network training dataset. Surprisingly, only a few of our coccolithophore bloom observations were flagged as out-of-range of the training dataset. Similarly, POLYMER converged in case-1 mode, using initial parameters for chlorophyll-*a* concentration and backscattering coefficients for case-1 water. As expected, given that our observations were of turbid case-2 water, neither of these algorithms performed well in the bloom compared to other algorithms, but it is concerning that neither algorithm reliably recognized the coccolithophore bloom observations as outside of its scope (C2RCC: MAE = 1.2, wins = 48%, POLYMER: MAE = 1.3, wins = 17%, Figure 10). Since both C2RCC and POLYMER will always return a modelled, realistic-looking reflectance spectrum, it is advisable to use these algorithms only within the known scope of their training dataset or model, and to thoroughly evaluate product flags.

There is a clear division between atmospheric correction algorithms that performed well in the turbid conditions of the 2022 bloom and those that did better with the lower signal recorded in April 2023. The L2gen algorithms belong to the first group, while POLYMER stood out as performing worst in 2022 and best in 2023. This result agrees with previous assessments of POLYMER being well-suited for clearer waters, but not performing

as well in turbid waters, likely because its water reflectance model cannot reproduce the reflectances of highly scattering coastal water [23,64,65]. In contrast, ACOLITE is generally found to perform well in very turbid coastal water [23,64]. In our study, unlike any other algorithm except the Rayleigh correction, ACOLITE consistently under-corrected satellite reflectances and showed a positive bias in both years (mean bias = 1.2 in 2022, mean bias = 1.9 in 2023). This could be because no sufficiently dark pixels were found in the chosen subset of the OLCI images, or because of strong atmospheric heterogeneity within the subset. BAC, the standard atmospheric correction used to generate the official Sentinel-3 OLCI Level-2 product, did not produce outstanding results in either turbid or clear conditions. Users of these products should be aware that other algorithms may be better suited for their study areas.

Few of the chlorophyll-*a* retrieval algorithms used in this study were able to return chlorophyll-*a* concentrations that matched our in situ measurements (Figures 12 and 13). The red-edge algorithms, especially, frequently produced negative values and extreme outliers. Most likely, chlorophyll-*a* concentrations were too low in both years to produce sufficient fluorescence peaks. Neither BAC nor C2RCC neural net output agreed well with in-situ chlorophyll-*a* during the coccolithophore bloom (BAC-NN: MAE = 3.5, wins = 14%, C2RCC-NN: MAE = 3.9, wins = 16%), as was to be expected, given that no neural nets trained on coccolithophore blooms were available at the time of this study. While one of the red-edge algorithms, from Mishra and Mishra (2012) [37], in combination with L2gen-corrected satellite reflectances performed best in the coccolithophore bloom (wins = 86.6%), OC5 (in combination with POLYMER) gave best results in 2023, when scattering and absorption were lower (wins = 93.8%).

The Sentinel-3 mission accuracy requirement for chlorophyll-*a* retrievals in case-2 water is 70% [59]. In the coccolithophore bloom, this threshold was reached for many retrievals, with the notable exception of both BAC and C2RCC Neural Net chlorophyll-*a* estimates (Figure 14). In 2023, few retrievals were below this threshold (Figure 15). These included POLYMER in combination with OC4 and OC5, as well as iCOR in combination with Moses et al. (2019) [38] and both iCOR and L2gen_MUMM in combination with Bramich et al. (2021) [35] and Gons et al. (2005) [36]. It should be noted that in contrast to POLYMER with OC4 and OC5, which retrieved valid chlorophyll-*a* concentrations for all 15 stations, these red-edge algorithms only made 5–6 valid chlorophyll-*a* retrievals. No combination of atmospheric correction and chlorophyll-*a* retrieval algorithms reached below the 10% accuracy goal defined in the Sentinel-3 mission requirements [59]. While these inaccuracies in chlorophyll-*a* retrieval may be partly due to errors in atmospheric correction, it should also be noted the chlorophyll-*a* algorithms tested here, even those designed for turbid waters, were generated from particle communities that differ from those observed in Norwegian fjords in phytoplankton species composition and presence of inorganic sediments. Especially coccolithophore blooms lie outside the scope of all the algorithms tested here.

Within the half-century since its inception, ocean color remote sensing has become indispensable to marine sciences and industries. Despite the uncertainties we still find in coastal products, not only within our study area, but globally, these products are being used in scientific studies and by industries and governments to inform decisions with consequences for economy and environment. Improving these products, especially those easily available to non-specialists, and extending the range of atmospheric correction and chlorophyll-*a* retrieval algorithms needs to remain a priority in our field. Users processing coastal remote sensing products need to be aware that their choice of algorithm both in atmospheric correction and retrieval of chlorophyll-*a* matters, and that algorithm performance changes not only regionally, but also seasonally, as observed here in measurements during and outside a coccolithophore bloom. Remote sensing observations of less well-studied optical environments, such as the coccolithophore bloom described here, may not yet be trustworthy without thorough validation through in situ measurements.

Supplementary Materials: The following supporting information can be downloaded at: https://www.mdpi.com/article/10.3390/rs16214082/s1.

Author Contributions: Conceptualization, E.T., B.H. and A.S.K.; Data curation, B.H. and A.S.K.; Formal analysis, E.T.; Funding acquisition, A.S.K.; Investigation, B.H. and A.S.K.; Methodology, E.T., B.H. and A.S.K.; Project administration, A.S.K.; Resources, B.H. and A.S.K.; Software, B.H.; Supervision, B.H. and A.S.K.; Visualization, E.T.; Writing—original draft, E.T.; Writing—review and editing, E.T., B.H. and A.S.K. All authors have read and agreed to the published version of the manuscript.

Funding: This work was funded by the Norwegian Research Council through the project "Enhanced Ocean Colour Remote Sensing for Optically Complex Waters" (Project Nr. 303190).

Data Availability Statement: The raw data supporting the conclusions of this article will be made available by the authors on request.

Acknowledgments: We thank the Norwegian coast guard and especially the crew of KV Tor for their vital support during the fieldwork. Special thanks also to the members of the Optics group and students at IFT who participated in the fieldwork.

Conflicts of Interest: The authors declare that the research was conducted in the absence of any commercial or financial relationships that could be construed as a potential conflict of interest.

References

1. Hovis, W.A.; Clark, D.K.; Anderson, F.; Austin, R.W.; Wilson, W.H.; Baker, E.T.; Ball, D.; Gordon, H.R.; Mueller, J.L.; El-Sayed, S.Z.; et al. Nimbus-7 Coastal Zone Color Scanner: System Description and Initial Imagery. *Science* **1980**, *210*, 60–63. [CrossRef] [PubMed]
2. Buhl-Mortensen, P.; Buhl-Mortensen, L. Diverse and Vulnerable Deep-Water Biotopes in the Hardangerfjord. *Mar. Biol. Res.* **2014**, *10*, 253–267. [CrossRef]
3. Manzetti, S.; Stenersen, J.H.V. A Critical View of the Environmental Condition of the Sognefjord. *Mar. Pollut. Bull.* **2010**, *60*, 2167–2174. [CrossRef] [PubMed]
4. Karlson, B.; Andersen, P.; Arneborg, L.; Cembella, A.; Eikrem, W.; John, U.; West, J.J.; Klemm, K.; Kobos, J.; Lehtinen, S.; et al. Harmful Algal Blooms and Their Effects in Coastal Seas of Northern Europe. *Harmful Algae* **2021**, *102*, 101989. [CrossRef] [PubMed]
5. Khan, R.M.; Salehi, B.; Mahdianpari, M.; Mohammadimanesh, F.; Mountrakis, G.; Quackenbush, L.J. A Meta-Analysis on Harmful Algal Bloom (Hab) Detection and Monitoring: A Remote Sensing Perspective. *Remote Sens.* **2021**, *13*, 4347. [CrossRef]
6. IOCCG. *Observation of Harmful Algal Blooms with Ocean Colour Radiometry*; Bernard, S., Lain, L.R., Kudela, R., Pitcher, G., Eds.; Reports of the International Ocean Colour Coordinating Group; IOCCG: Dartmouth, NS, Canada, 2021; Volume 20.
7. IOCCG. *Atmospheric Correction for Remotely-Sensed Ocean-Colour Products*; Wang, M., Ed.; Reports of the International Ocean Colour Coordinating Group; IOCCG: Dartmouth, NS, Canada, 2010; Volume 10.
8. Gordon, H.R. Evolution of Ocean Color Atmospheric Correction: 1970–2005. *Remote Sens.* **2021**, *13*, 5051. [CrossRef]
9. Werdell, P.J.; McKinna, L.I.W.; Boss, E.; Ackleson, S.G.; Craig, S.E.; Gregg, W.W.; Lee, Z.; Maritorena, S.; Roesler, C.S.; Rousseaux, C.S.; et al. An Overview of Approaches and Challenges for Retrieving Marine Inherent Optical Properties from Ocean Color Remote Sensing. *Prog. Oceanogr.* **2018**, *160*, 186–212. [CrossRef]
10. Mobley, C.D.; Stramski, D.; Paul Bissett, W.; Boss, E. Optical Modeling of Ocean Waters: Is the Case 1–Case 2 Classification Still Useful? *Oceanography* **2004**, *17*. [CrossRef]
11. Gordon, H.R.; Wang, M. Retrieval of Water-Leaving Radiance and Aerosol Optical Thickness over the Oceans with SeaWiFS: A Preliminary Algorithm. *Appl. Opt.* **1994**, *33*, 443–452. [CrossRef]
12. Antoine, D. OLCI Level 2 Algorithm Theoretical Basis Document: Atmospheric Corrections over Case 1 Waters (CWAC). Ref S3-L2-SD-03-C07-LOV-ATBD Version 22. 2010. Available online: https://sentiwiki.copernicus.eu/__attachments/1672112/S3-L2-SD-03-C07-LOV-ATBD%20-%20OLCI%20L2%20ATBD%20Atmospheric%20Corrections%20case%201%20waters%202010%20-%2002.pdf?inst-v=d105f701-8f35-4a57-9bd3-983ac5f50bca (accessed on 28 October 2024).
13. Mazeran, C.; Hieronymi, M.; Steinmetz, F. Ocean Colour Bright Pixel Correction–Algorithm Theoretical Basis. EUM/18/BPC/ATBD. 2021. Available online: https://www-cdn.eumetsat.int/files/2021-10/S3-OLCI_OC-BPC_ATBD.pdf (accessed on 28 October 2024).
14. Vanhellemont, Q.; Ruddick, K. Atmospheric Correction of Metre-Scale Optical Satellite Data for Inland and Coastal Water Applications. *Remote Sens. Environ.* **2018**, *216*, 586–597. [CrossRef]
15. Brockmann, C.; Doerffer, R.; Peters, M.; Stelzer, K.; Embacher, S.; Ruescas, A. *Evolution of the C2RCC Neural Network for Sentinel 2 and 3 for the Retrieval of Ocean Colour Products in Normal and Extreme Optically Complex Waters*; European Space Agency: Paris, France, 2016; Volume SP-740.

16. De Keukelaere, L.; Sterckx, S.; Adriaensen, S.; Knaeps, E.; Reusen, I.; Giardino, C.; Bresciani, M.; Hunter, P.; Neil, C.; Van der Zande, D.; et al. Atmospheric Correction of Landsat-8/OLI and Sentinel-2/MSI Data Using iCOR Algorithm: Validation for Coastal and Inland Waters. *Eur. J. Remote Sens.* **2018**, *51*, 525–542. [CrossRef]
17. Bailey, S.W.; Franz, B.A.; Werdell, P.J. Estimation of Near-Infrared Water-Leaving Reflectance for Satellite Ocean Color Data Processing. *Opt. Express* **2010**, *18*, 7521–7527. [CrossRef] [PubMed]
18. Wang, M.; Son, S.; Shi, W. Evaluation of MODIS SWIR and NIR-SWIR Atmospheric Correction Algorithms Using SeaBASS Data. *Remote Sens. Environ.* **2009**, *113*, 635–644. [CrossRef]
19. Ruddick, K.G.; Ovidio, F.; Rijkeboer, M. Atmospheric Correction of SeaWiFS Imagery for Turbid Coastal and Inland Waters. *Appl. Opt.* **2000**, *39*, 897–912. [CrossRef] [PubMed]
20. Steinmetz, F.; Ramon, D. Sentinel-2 MSI and Sentinel-3 OLCI Consistent Ocean Colour Products Using POLYMER. In *Remote Sensing of the Open and Coastal Ocean and Inland Waters*; SPIE: Bellingham, WA, USA, 2018; Volume 13. [CrossRef]
21. Steinmetz, F.; Deschamps, P.-Y.; Ramon, D. Atmospheric Correction in Presence of Sun Glint: Application to MERIS. *Opt. Express* **2011**, *19*, 9783. [CrossRef]
22. Park, Y.-J.; Ruddick, K. Model of Remote-Sensing Reflectance Including Bidirectional Effects for Case 1 and Case 2 Waters. *Appl. Opt.* **2005**, *44*, 1236–1249. [CrossRef]
23. Vanhellemont, Q.; Ruddick, K. Atmospheric Correction of Sentinel-3/OLCI Data for Mapping of Suspended Particulate Matter and Chlorophyll-a Concentration in Belgian Turbid Coastal Waters. *Remote Sens. Environ.* **2021**, *256*, 112284. [CrossRef]
24. Bourg, L. MERIS Level 2 Detailed Processing Model. In *Document no. PO-TN-MEL-GS-0006*; ACRI-ST, 2011; Available online: https://earth.esa.int/eogateway/documents/20142/37627/MERIS-Level-2-Detailed-Processing-Model.pdf/075b5eb1-7b3b-52f5-28a4-9fbb5d8e0fb7?t=1703157756360 (accessed on 28 October 2024).
25. Brewin, R.J.W.; Sathyendranath, S.; Müller, D.; Brockmann, C.; Deschamps, P.-Y.; Devred, E.; Doerffer, R.; Fomferra, N.; Franz, B.; Grant, M.; et al. The Ocean Colour Climate Change Initiative: III. A Round-Robin Comparison on in-Water Bio-Optical Algorithms. *Remote Sens. Environ.* **2015**, *162*, 271–294. [CrossRef]
26. Balch, W.M.; Gordon, H.R.; Bowler, B.C.; Drapeau, D.T.; Booth, E.S. Calcium Carbonate Measurements in the Surface Global Ocean Based on Moderate-Resolution Imaging Spectroradiometer Data. *J. Geophys. Res. C Oceans* **2005**, *110*, 1–21. [CrossRef]
27. Ansper, A.; Alikas, K. Retrieval of Chlorophyll a from Sentinel-2 MSI Data for the European Union Water Framework Directive Reporting Purposes. *Remote Sens.* **2019**, *11*, 64. [CrossRef]
28. Pahlevan, N.; Mangin, A.; Balasubramanian, S.V.; Smith, B.; Alikas, K.; Arai, K.; Barbosa, C.; Bélanger, S.; Binding, C.; Bresciani, M.; et al. ACIX-Aqua: A Global Assessment of Atmospheric Correction Methods for Landsat-8 and Sentinel-2 over Lakes, Rivers, and Coastal Waters. *Remote Sens. Environ.* **2021**, *258*, 112366. [CrossRef]
29. Wang, D.; Ma, R.; Xue, K.; Loiselle, S.A. The Assessment of Landsat-8 OLI Atmospheric Correction Algorithms for Inland Waters. *Remote Sens.* **2019**, *11*, 169. [CrossRef]
30. Windle, A.E.; Evers-King, H.; Loveday, B.R.; Ondrusek, M.; Silsbe, G.M. Evaluating Atmospheric Correction Algorithms Applied to OLCI Sentinel-3 Data of Chesapeake Bay Waters. *Remote Sens.* **2022**, *14*, 1881. [CrossRef]
31. Maciel, F.P.; Pedocchi, F. Evaluation of ACOLITE Atmospheric Correction Methods for Landsat-8 and Sentinel-2 in the Río de La Plata Turbid Coastal Waters. *Int. J. Remote Sens.* **2022**, *43*, 215–240. [CrossRef]
32. Bendif, E.M.; Nevado, B.; Wong, E.L.Y.; Hagino, K.; Probert, I.; Young, J.R.; Rickaby, R.E.M.; Filatov, D.A. Repeated Species Radiations in the Recent Evolution of the Key Marine Phytoplankton Lineage Gephyrocapsa. *Nat. Commun.* **2019**, *10*, 4234. [CrossRef]
33. Tyrrell, T.; Merico, A. Emiliania Huxleyi: Bloom Observations and the Conditions That Induce Them. In *Coccolithophores: From Molecular Processes to Global Impact*; Springer: Berlin/Heidelberg, Germany, 2004; pp. 75–97.
34. Berge, G. Discoloration of the Sea Due to Coccolithus Huxleyi "Bloom". *Sarsia* **1962**, *6*, 27–40. [CrossRef]
35. Bramich, J.; Bolch, C.J.S.; Fischer, A. Improved Red-Edge Chlorophyll-a Detection for Sentinel 2. *Ecol. Indic.* **2021**, *120*, 106876. [CrossRef]
36. Gons, H.J.; Rijkeboer, M.; Ruddick, K.G. Effect of a Waveband Shift on Chlorophyll Retrieval from MERIS Imagery of Inland and Coastal Waters. *J. Plankton Res.* **2005**, *27*, 125–127. [CrossRef]
37. Mishra, S.; Mishra, D.R. Normalized Difference Chlorophyll Index: A Novel Model for Remote Estimation of Chlorophyll-a Concentration in Turbid Productive Waters. *Remote Sens. Environ.* **2012**, *117*, 394–406. [CrossRef]
38. Moses, W.J.; Saprygin, V.; Gerasyuk, V.; Povazhnyy, V.; Berdnikov, S.; Gitelson, A.A. OLCI-Based NIR-Red Models for Estimating Chlorophyll-a Concentration in Productive Coastal Waters—A Preliminary Evaluation. *Environ. Res. Commun.* **2019**, *1*, 011002. [CrossRef]
39. O'Reilly, J.E.; Werdell, P.J. Chlorophyll Algorithms for Ocean Color Sensors–OC4, OC5 & OC6. *Remote Sens. Environ.* **2019**, *229*, 32–47. [CrossRef] [PubMed]
40. Hamre, B.; Stamnes, S.; Stamnes, K.; Stamnes, J. AccuRT: A Versatile Tool for Radiative Transfer Simulations in the Coupled Atmosphere-Ocean System. *AIP Conf. Proc.* **2017**, *1810*, 120002. [CrossRef]
41. Burggraaff, O. Biases from Incorrect Reflectance Convolution. *Opt. Express* **2020**, *28*, 13801–13816. [CrossRef] [PubMed]
42. Tassan, S.; Ferrari, G.M. A Sensitivity Analysis of the 'Transmittance–Reflectance'Method for Measuring Light Absorption by Aquatic Particles. *J. Plankton Res.* **2002**, *24*, 757–774. [CrossRef]

43. Van Heukelem, L.; Thomas, C.S. Computer-Assisted High-Performance Liquid Chromatography Method Development with Applications to the Isolation and Analysis of Phytoplankton Pigments. *J. Chromatogr. A* **2001**, *910*, 31–49. [CrossRef]
44. Holm-Hansen, O.; Riemann, B. Chlorophyll a Determination: Improvements in Methodology. *Oikos* **1978**, 438–447. [CrossRef]
45. Seegers, B.N.; Stumpf, R.P.; Schaeffer, B.A.; Loftin, K.A.; Werdell, P.J. Performance Metrics for the Assessment of Satellite Data Products: An Ocean Color Case Study. *Opt. Express* **2018**, *26*, 7404–7422. [CrossRef]
46. EUMETSAT. *Recommendations for Sentinel-3 OLCI Ocean Colour Product Validations in Comparison with in Situ Measurements – Matchup Protocols*. 2022. Available online: https://user.eumetsat.int/s3/eup-strapi-media/Recommendations_for_Sentinel_3_OLCI_Ocean_Colour_product_validations_in_comparison_with_in_situ_measurements_Matchup_Protocols_V8_B_e6c62ce677.pdf (accessed on 28 October 2024).
47. Ahmad, Z.; Franz, B.A.; McClain, C.R.; Kwiatkowska, E.J.; Werdell, J.; Shettle, E.P.; Holben, B.N. New Aerosol Models for the Retrieval of Aerosol Optical Thickness and Normalized Water-Leaving Radiances from the SeaWiFS and MODIS Sensors over Coastal Regions and Open Oceans. *Appl. Opt.* **2010**, *49*, 5545–5560. [CrossRef]
48. Wang, M.; Shi, W. The NIR-SWIR Combined Atmospheric Correction Approach for MODIS Ocean Color Data Processing. *Opt. Express* **2007**, *15*, 15722–15733. [CrossRef]
49. Doerffer, R. OLCI L2 ATBD Ocean Colour Turbid Water. Ref S3-L2-SD-03-C11-GKSS-ATBD Version 20. 2010. Available online: https://step.esa.int/docs/extra/OLCI_L2_ATBD_Ocean_Colour_Turbid_Water.pdf (accessed on 28 October 2024).
50. Sterckx, S.; Knaeps, S.; Kratzer, S.; Ruddick, K. SIMilarity Environment Correction (SIMEC) Applied to MERIS Data over Inland and Coastal Waters. *Remote Sens. Environ.* **2015**, *157*, 96–110. [CrossRef]
51. Berk, A.; Anderson, G.P.; Acharya, P.K.; Bernstein, L.S.; Muratov, L.; Lee, J.; Fox, M.; Adler-Golden, S.M.; Chetwynd, J.H., Jr.; Hoke, M.L. MODTRAN5: 2006 Update. In *Algorithms and Technologies for Multispectral, Hyperspectral, and Ultraspectral Imagery XII*; SPIE: Bellingham, WA, USA, 2006; Volume 6233, pp. 508–515.
52. Morel, A.; Antoine, D.; Gentili, B. Bidirectional Reflectance of Oceanic Waters: Accounting for Raman Emission and Varying Particle Scattering Phase Function. *Appl. Opt.* **2002**, *41*, 6289–6306. [CrossRef] [PubMed]
53. EUMETSAT. Sentinel-3 OLCI L2 Report for Baseline Collection OL_L2M_003. 2021. Available online: https://user.eumetsat.int/s3/eup-strapi-media/Sentinel_3_OLCI_L2_report_for_baseline_collection_OL_L2_M_003_2_B_c8bbc6d986.pdf (accessed on 28 October 2024).
54. Franz, B.A.; Bailey, S.W.; Werdell, P.J.; McClain, C.R. Sensor-Independent Approach to the Vicarious Calibration of Satellite Ocean Color Radiometry. *Appl. Opt.* **2007**, *46*, 5068–5082. [CrossRef] [PubMed]
55. Gons, H.J.; Rijkeboer, M.; Ruddick, K.G. A Chlorophyll-Retrieval Algorithm for Satellite Imagery (Medium Resolution Imaging Spectrometer) of Inland and Coastal Waters. *J. Plankton Res.* **2002**, *24*, 947–951. [CrossRef]
56. Gons, H.J.; Auer, M.T.; Effler, S.W. MERIS Satellite Chlorophyll Mapping of Oligotrophic and Eutrophic Waters in the Laurentian Great Lakes. *Remote Sens. Environ.* **2008**, *112*, 4098–4106. [CrossRef]
57. Bricaud, A.; Morel, A.; Prieur, L. Absorption by Dissolved Organic Matter of the Sea (Yellow Substance) in the UV and Visible Domains. *Limnol Ocean.* **1981**, *26*, 43–53. [CrossRef]
58. Moses, W.J.; Gitelson, A.A.; Berdnikov, S.; Saprygin, V.; Povazhnyi, V. Operational MERIS-Based NIR-Red Algorithms for Estimating Chlorophyll-a Concentrations in Coastal Waters–The Azov Sea Case Study. *Remote Sens. Environ.* **2012**, *121*, 118–124. [CrossRef]
59. Drinkwater, M.; Rebhan, H. Sentinel-3: Mission Requirements Document. Ref EOP-SMO1151MD-Md 2007. Available online: https://earth.esa.int/eogateway/documents/20142/1564943/Sentinel-3-Mission-Requirements-Document-MRD.pdf (accessed on 28 October 2024).
60. Moore, T.S.; Dowell, M.D.; Franz, B.A. Detection of Coccolithophore Blooms in Ocean Color Satellite Imagery: A Generalized Approach for Use with Multiple Sensors. *Remote Sens. Environ.* **2012**, *117*, 249–263. [CrossRef]
61. Brown, C.W.; Yoder, J.A. Coccolithophorid Blooms in the Global Ocean. *J. Geophys. Res. Oceans* **1994**, *99*, 7467–7482. [CrossRef]
62. Garcia, C.A.E.; Garcia, V.M.T.; Dogliotti, A.I.; Ferreira, A.; Romero, S.I.; Mannino, A.; Souza, M.S.; Mata, M.M. Environmental Conditions and Bio-optical Signature of a Coccolithophorid Bloom in the Patagonian Shelf. *J. Geophys. Res. Oceans* **2011**, *116*. [CrossRef]
63. Siegel, H.; Ohde, T.; Gerth, M.; Lavik, G.; Leipe, T. Identification of Coccolithophore Blooms in the SE Atlantic Ocean off Namibia by Satellites and In-Situ Methods. *Cont. Shelf Res.* **2007**, *27*, 258–274. [CrossRef]
64. Renosh, P.R.; Doxaran, D.; Keukelaere, L.D.; Gossn, J.I. Evaluation of Atmospheric Correction Algorithms for Sentinel-2-MSI and Sentinel-3-OLCI in Highly Turbid Estuarine Waters. *Remote Sens.* **2020**, *12*, 1285. [CrossRef]
65. Warren, M.A.; Simis, S.G.H.; Martinez-Vicente, V.; Poser, K.; Bresciani, M.; Alikas, K.; Spyrakos, E.; Giardino, C.; Ansper, A. Assessment of Atmospheric Correction Algorithms for the Sentinel-2A MultiSpectral Imager over Coastal and Inland Waters. *Remote Sens. Environ.* **2019**, *225*, 267–289. [CrossRef]

Disclaimer/Publisher's Note: The statements, opinions and data contained in all publications are solely those of the individual author(s) and contributor(s) and not of MDPI and/or the editor(s). MDPI and/or the editor(s) disclaim responsibility for any injury to people or property resulting from any ideas, methods, instructions or products referred to in the content.